

Int. Journal of Heat and Mass Transfer, 140, pp. 100-128, 2019

**FLOW BOILING OF HFE-7100 IN MICROCHANNELS:
EXPERIMENTAL STUDY AND COMPARISON WITH
CORRELATIONS**

Ali H. Al-Zaidi^{1,2}, Mohamed M. Mahmoud³, Tassos G. Karayiannis^{1*}

*¹Department of Mechanical and Aerospace Engineering, Brunel University London, Uxbridge,
UB8 3PH, UK*

²University of Misan, Al-Amarah, 62001, Iraq

³Faculty of Engineering, Zagazig University, Zagazig, 44519, Egypt

*Address correspondence to Prof. Tassos G. Karayiannis, Department of Mechanical and Aerospace Engineering, Brunel University London, Uxbridge, Middlesex, UB8 3PH, UK.

Email: tassos.karayiannis@brunel.ac.uk

Phone Number: +44 (0) 1895 267132, Fax Number: +44 (0)1895 256392

Abstract

The main objective of this research was the design and test of a multi-microchannels heat sink for electronics cooling applications, which operates at system pressure near atmospheric and low mass flow rates. HFE-7100, a dielectric and eco-friendly coolant, was chosen as the working fluid. Twenty five rectangular microchannels, of width 0.7 mm and height 0.35 mm giving a hydraulic diameter of 0.46 mm, were fabricated from oxygen-free copper with a base area of 500 mm². The channels in-between wall was 0.1 mm thick. Five mass fluxes ranging from 50 to 250 kg/m²s were tested at fixed inlet sub-cooling near 5 K. The effect of heat flux, mass flux and vapour quality on the local heat transfer coefficient was investigated. Four flow patterns namely; bubbly, slug, churn and annular flow, were visualized using a high-speed camera mounted on a microscope. In this study, the maximum flow boiling heat transfer coefficient was 12.71 kW/m²K at mass flux of 250 kg/m²s. A comprehensive comparison with experimental results was conducted including flow pattern maps, heat transfer and pressure drop correlations. Some of the correlations, proposed for conventional channels and microchannels, showed good agreement with the present results.

Keywords: Flow boiling, microchannel, flow patterns, heat transfer coefficient, pressure drop, correlations, flow reversal, electronics cooling.

1. Introduction

Flow boiling in micro scale heat sinks, as part of small-scale thermal management systems, is a promising solution for cooling electronic components. This is due to the liquid to vapour change process accompanied with high heat transfer coefficients and consequently the possibility to dissipate high heat fluxes from a small area. Generally, flow boiling heat sinks consist of multi-microchannels and can be attached to the chipset, as shown in Fig. 1. In a cooling system driven with a pump, the coolant enters the heat sink at a sub-cooled state and leaves either as saturated vapour or as a mixture of liquid and vapour. However, this technique is not widely used as yet in commercial applications due to the lack of understanding of several fundamental and design issues. Cheng and Xia [1] conducted a review study on the fundamental issues, heat transfer mechanism(s) and correlations of flow boiling heat transfer in microchannels. They compared twelve existing heat transfer correlations and two mechanistic models with 2336 data points collected from literature. The collected database included 8 fluids, channel diameter ranging from 0.19 to 3.69 mm and horizontal and vertical orientations. They reported that the correlations and models were not able to predict all data with a reasonable accuracy, and thus it was concluded that there are no universal correlations for flow boiling heat transfer in microchannels. They recommended that flow boiling mechanisms, flow patterns, fluid properties and channel size should be considered when a new prediction correlation or model is developed. Additionally, it was concluded that there is a large discrepancy among the published experimental results even at the same experimental conditions. The possible reasons of discrepancies in the past studies were discussed in Karayiannis et al. [2]. They studied the effect of test section surface microstructure and heated length on the local heat transfer characteristics and found that the variations in these two factors resulted in significant variations in the local heat transfer coefficient. This can explain the reported discrepancies among researchers. Karayiannis and Mahmoud [3-5] presented detailed discussions on several fundamental aspects of flow boiling in microchannels and also presented possible applications. They concluded that there is no common agreement among researchers on (i) the definition of microchannel, (ii) the dominant heat transfer mechanism(s), (iii) the prediction of heat transfer coefficient, critical heat flux (CHF) and flow pattern transition boundaries. They reported that both nucleate and convective boiling mechanisms contribute to the heat transfer rates in microchannels and it is difficult to segregate the contribution of each mechanism. They attributed the discrepancy among researchers on the dominant heat transfer mechanism(s) to the complex dependency of the heat transfer rates on flow patterns, channel surface finish, geometry, channel length, fluid properties and experimental/operating conditions.

Flow boiling in microchannels using the dielectric coolant HFE-7100 is considered a suitable choice for electronics cooling applications. In the following paragraphs, the flow boiling characteristics in microchannels are reviewed only for HFE-7100, which is more relevant to the current study. Lee and Mudawar [6-8] conducted an experimental investigation of flow boiling heat transfer of HFE-7100 in four horizontal rectangular multi-microchannels made of oxygen-free copper, with hydraulic diameter ranging from 0.176 to 0.416 mm and aspect ratio (width to height) range of 0.25–0.41. They conducted

their study at very low inlet coolant temperature, i.e. 0 and -30 °C, and high mass fluxes, ranging from 670 to 6730 kg/m²s. They reported that the critical heat flux could be enhanced by decreasing the coolant temperature, i.e. increasing the inlet sub-cooling. The onset of nucleate boiling was delayed and the bubble departure size was reduced with decreasing coolant temperature. In their study, the maximum attainable heat flux was as high as 7000 kW/m². Additionally, they reported that the heat sink with smaller hydraulic diameter exhibited better heat transfer performance compared to channels with large diameters. This was attributed to an increase in the wetted area and mass velocity for the small hydraulic diameter. However, the effect of diameter was studied while the channel aspect ratio was not fixed. In other words, the change in the wetted area could be due to a change in the aspect ratio rather than a change in diameter. Also, it is worth mentioning that, the flow pattern was only discrete bubbly flow, i.e. a case of highly sub-cooled boiling.

Yang et al. [9] studied flow patterns and heat transfer rates of HFE-7100 in copper multi-microchannels with hydraulic diameter of 0.48 and 0.79 mm. Their experiments were performed at a system pressure of 1 bar, mass flux range 100–400 kg/m²s and two heat fluxes of 25 and 37.5 kW/m². Their flow visualization showed that churn/annular flow was the dominant regime in the smaller channel, while there was a progression of flow regimes from bubbly to elongated bubble, slug and churn/annular flows in the larger channel with increasing heat flux. They also found that flow reversal occurred in the smaller channel at higher heat flux and mass flux of 100 kg/m²s, while it was not observed in the larger one. The authors did not give a reason for this difference. The heat transfer results demonstrated that the heat transfer coefficient in the small channel was always greater than that found in the large channel at all operating conditions. In the 0.48 mm diameter channel at mass flux of 200–400 kg/m²s, the heat transfer coefficient was roughly independent of vapour quality and heat flux. Contrary to that, the heat transfer coefficient in the 0.79 mm diameter channel increased with heat flux up to vapour quality of about 0.4. Moreover, for both channels, the effect of mass flux on the heat transfer coefficient was insignificant. The noticeable heat flux effect in the large channel was attributed to the presence of bubbly and slug flows that promoted nucleate boiling mechanism. On the contrary, the insignificant heat flux effect in the small channel was attributed to the dominance of annular flow that promoted thin film evaporation and consequently the dominance of convective boiling mechanism. It is worth mentioning that, there was no heat flux effect in the large channel at $G = 100$ kg/m²s and there was a deterioration in the heat transfer coefficient in the small channel, which was attributed to flow reversal. Yang et al. [10] carried out an experimental investigation on flow boiling heat transfer of HFE-7000 in a silicon multi-microchannel heat sink consisting of five parallel channels with height of 0.25 mm and width of 0.22 mm. Two types of channels were tested, namely plain-wall and nanostructured channels. The bottom and sidewalls of these nanostructured channels were modified using a nanowires structure of height 5 μm and diameter of 0.02–0.1 μm. A metal-assisted chemical etching process was used to modify these channels. The mass flux ranged from 1018 to 2206 kg/m²s.

They reported that the heat transfer coefficient increased by 344% in the nanostructured channels compared to the plain-wall channels. The critical heat flux was enhanced by 14.9% (from 920 to 1200 kW/m²) and the pumping power decreased by 40% for the nanostructured surface. It is worth mentioning that, the highest enhancement in heat transfer coefficient and highest reduction in pumping power was achieved with the lowest mass flux $G = 1018 \text{ kg/m}^2\text{s}$. With an increase in mass flux to 1527 kg/m²s, the reduction in pumping power was only 17.9%. At mass flux above 1527 kg/m²s, the pumping power for the nanostructured channels was found to be higher than that in plain-wall channels. The authors attributed this to the high flow resistance as a result of high surface roughness of the modified channels, i.e. the nano-structured walls [10]. The reported heat transfer enhancements in the nanostructured channels were attributed by [10] to the dominance of annular flow induced by the capillary effects for $x < 0.11$ (thin film evaporation) and the activation of more nucleation sites at higher vapour quality (high heat flux).

Fu et al. [11] studied the effect of channel structure on flow boiling heat transfer of HFE-7100 in a horizontal copper multi-channel heat sink consisting of four minichannels with 2 mm height and 0.5 mm width. Two types of channel surface structure were tested, namely a plain surface and a surface modified by saw tooth structure fabricated by wire-cut electrical machine. The channels with saw tooth structure were tested with two flow configurations. The first was called parallel flow (along the teeth inclination) and the second was called counter flow, against the angle of teeth direction. It was found that the flow direction has an insignificant effect on the CHF for the tested channels with saw tooth structure. At small mass flux, the CHF increased by 44% for the parallel tooth channels compared to the plain channels. The enhancement in CHF due the channel modification was found to decrease with increasing mass flux.

Fu et al. [12] examined the effect of aspect ratio on flow boiling heat transfer of HFE-7100 in horizontal diverging multi-microchannels made of copper with a fixed hydraulic diameter of 1.12 mm. Six channels with different aspect ratio (width to height) of 0.16, 0.23, 0.4, 0.6, 1 and 1.2 were tested. They conducted their experiments at a mass flux of 39, 55, 78, 90 and 180 kg/m²s. Their results showed that the heat transfer coefficient decreased from a maximum value at very low vapour quality up to $x = 0.4-0.6$ after which the heat transfer coefficient did not vary with vapour quality. It is worth mentioning that, their figures indicate that the effect of aspect ratio did not show a specific trend. However, the channels with aspect ratio of one exhibited the best heat transfer performance (CHF and heat transfer coefficient) as they reported. This was attributed by [12] to the existence of the liquid film around the channel corners in the square channel, i.e. all walls were wetted. The lower heat transfer coefficient in the channels with other aspect ratios was attributed to the possibility of partial dryout (non-wetted walls).

The effect of orientation on flow boiling of HFE-7100 was studied by Wang et al. [13] and Hsu [14]. Wang et al. studied the effect of channel inclination, from 90° (vertical-upward flow) to -90° (vertical-downward flow), with a copper multi-microchannel heat sink having a hydraulic diameter of 0.825 mm.

Three different mass fluxes, 100, 200 and 300 kg/m²s, and two heat fluxes of 25 and 37.5 kW/m² at system pressure of 1 bar were tested. They reported that the heat transfer coefficient was nearly independent of vapour quality. They found that for $G = 100 \text{ kg/m}^2\text{s}$, the heat transfer coefficient increased by 30% for upward inclination angle of 45° compared to the horizontal orientation. The heat transfer coefficient decreased with further increase in inclination to 90°. The downward inclination angles resulted in a lower heat transfer coefficients compared to the upward orientation. This was attributed to the increase in the velocity of the vapour slug due to the buoyancy effect and the symmetrical shape of the elongated bubble with uniform liquid film encountered with the upward inclination. Hsu et al. [14] used the same experimental facility for channels with hydraulic diameter 0.44 mm. They reported that, for $q = 25 \text{ kW/m}^2$, the average heat transfer coefficient increased with vapour quality up to 0.6 for all orientations except the horizontal and considered this behaviour as an indication of convective boiling. After vapour quality value of 0.6, the heat transfer coefficient decreased with quality for all orientations, which was attributed by [14] to partial dryout. For $q = 40 \text{ kW/m}^2$ and quality less than 0.6, the average heat transfer coefficient was independent of vapour quality. This was considered by [14] as an indication of the dominance of nucleate boiling. Their results showed that the heat transfer coefficient for the upward orientations was higher than those of the downward flow orientations, especially at low mass fluxes. The effect of orientation diminished as the mass flux increased.

As summarised above, several studies on flow boiling of HFE-7100 in microchannels were conducted in the last few years. However, there are still some fundamental issues that still need to be clarified, such as effect of operating parameters, prediction correlations, dominant heat transfer mechanism(s) and flow instability. Additionally, there is a lack of flow patterns data for this fluid. In most previous studies, the results were presented as average heat transfer coefficient versus exit vapour quality and there is no data for the local heat transfer coefficient versus local vapour quality, especially at low mass fluxes. Presenting the data as local heat transfer coefficient versus local quality combined with flow visualization may help explain the complex influence of the operating parameters on heat transfer rates and pressure drop of HFE-7100. In some studies, high mass fluxes and/or high inlet sub-cooling were used to achieve high heat fluxes. In the present study, HFE-7100 (3M Novec coolant) was chosen as the working fluid due to its saturation temperature at low pressures (59.6 °C at 1 bar), high dielectric strength and low global warming potential. This saturation temperature makes it possible to design a small system for electronics cooling with a small size condenser. The thermophysical properties of this coolant at 1 bar are presented in Table 1. System pressure near atmospheric and relatively low flow rates was examined. The tested heat sink is a part of small-scale thermal management system for cooling electronics components. In such systems, the size of the condenser can be significant compared to the evaporator. The inlet sub-cooling at the evaporator was set at low value, i.e. 5 K. In a real system this can help keep the condenser size as small as possible, reducing the overall system size/weight and pumping power consumption. Flow visualization and local heat transfer

calculations were obtained along the channels. The experimental results were used to compare and evaluate three flow pattern maps, fifteen heat transfer correlations and ten pressure drop correlations reported in the literature. Conclusions from these comparisons are given to highlight design equations.

2. Experimental system

2.1 Flow loop

A schematic diagram of the experimental facility is depicted in Fig. 2. This was described in detail by Al-Zaidi et al. [15]. This rig consisted of two main parts; the test loop and an auxiliary cooling loop. The test loop consisted of liquid reservoir (9 L volume), sub-cooler, micro-gear pump (with a flow rate up to 2304 mL/min), two Coriolis flow meters (for high and low flow rates), pre-heater with input power of 1500 W and the microchannel evaporator test section. Three Variac transformers were used to control the input power to the test section, the pre-heater and the liquid reservoir, i.e. control the heat flux, inlet sub-cooling and system pressure, respectively. The fluid flow rate during the experiments was controlled by a high precision digital driver connected to the micro-gear pump. A Phantom high-speed camera (1000 frames per second at 512×512 pixel) mounted on a microscope and LED lighting system was used to capture the flow patterns. The auxiliary cooling loop was a re-circulating chiller system with cooling capacity of 2.9 kW. It was used to reject the heat from the reservoir, the sub-cooler and the test section during the experiments. All the measuring instruments, pressure transducers, thermocouples and flow meters, were connected to the data logger (National Instruments Data Acquisition System-DAQ). This logger was connected to a computer with LabVIEW software to record and save all the measured data after the system reached steady state, i.e. small variations in pressure, temperature and mass flux. The data were saved for 2 min, i.e. 120,000 data were recorded, and then averaged for further calculations in the data reduction process.

2.2 Test section

The test section consisted of four main parts, namely; bottom plate, housing, cover plate and the heat sink block as shown in Fig. 3(a). The bottom plate and the housing were made of a Polytetrafluoroethylene block to ensure good insulation of the test section. Twelve holes with a diameter of 0.6 mm were drilled into the housing to pass the thermocouple wires through this part. A transparent polycarbonate sheet was used to fabricate the cover plate and allowed observation of the flow patterns. This plate was clamped on the topside of the housing and the inlet and outlet plenum (semi-circular shape) were formed in this part. Moreover, six tapping holes were drilled into this plate to connect the inlet and outlet flow tube, T-type thermocouples for inlet and outlet fluid temperature and the inlet, outlet and differential pressure transducers. The total pressure drop was measured directly across the heat sink (from inlet to outlet plenum) using one differential pressure transducer. An O-ring seal was inserted in a slot between the cover plate and the microchannel heat sink to prevent any possible fluid leakage. An oxygen-free copper block was used to manufacture the heat sink block, which had a width, height and

length of 26, 94.5 and 51 mm, respectively as shown in Fig. 3(b). A high-precision milling machine (Kern HSPC-2216) at a cutting feed rate of 550 mm/min and rotation speed of 20,000 rpm was used to fabricate twenty five rectangular microchannels on the upper surface of this block. It is worth mentioning that, the cutting feed rate and speed affect the channel surface microstructure and the surface roughness. The average surface roughness was measured using a surface profiler instrument (Zygo NewView 5000) for the bottom surface of a number of channels and the average value was 0.304 μm . The dimensions of these channels were 0.35 mm height, 0.7 mm width and 25 mm long, while the wall thickness between the channels was 0.1 mm as shown in Fig. 3(b) and Table 2. The microchannels and the inlet and outlet plenum (semi-circular shape) were fabricated as one part, i.e. a real microchannel heat sink. This design is acceptable for commercial applications since all parts, i.e. the heat sink and the cover plate, can easily be assembled and attached to the chipset.

The heat sink structure included the microchannels, the inlet and outlet plenum and the heating block. 12 K-type thermocouples were inserted into this block to measure the temperature distribution along the channels and in the vertical direction. The thermocouples were distributed as follows: (i) six thermocouples were inserted underneath the channels in the axial direction in two opposite rows with three thermocouples per row. The first row represented the mid plane of the heat sink while the second represented the side plane. This help estimate the uniformity of the heat flux. (ii) Another horizontal row of three thermocouples was inserted below the top row at 10 mm vertical distance to make sure that there is no axial heat conduction, i.e. our case is 1D heat conduction. (iii) Three additional thermocouples were inserted vertically (normal to the flow direction) in the heater block for the heat flux estimation. It is worth mentioning that, five vertical thermocouples in total were used to estimate the heat flux (two from the top rows and the three additional). Four vertical holes were drilled into the bottom side of the heating block to insert four cartridge heaters with total heating power of 700 W.

3. Data reduction

The fanning friction factor during the single-phase experiments is calculated using Eq. (1).

$$f_{exp} = \frac{\Delta P_{ch} D_h}{2 L_{ch} v_l G_{ch}^2} \quad (1)$$

ΔP_{ch} is the channel pressure drop, which is obtained from Eq. (2) below.

$$\Delta P_{ch} = \Delta P_{meas} - (\Delta P_{ip} + \Delta P_{sc} + \Delta P_{se} + \Delta P_{op}) \quad (2)$$

ΔP_{meas} , ΔP_{ip} , ΔP_{sc} , ΔP_{se} and ΔP_{op} are the total measured pressure drop along the channel (from the differential pressure transducer), the pressure drop in the inlet plenum due to the change in flow direction by 90°, the sudden contraction pressure drop at the channel inlet, the sudden expansion pressure drop at the channel outlet and the pressure drop in the outlet plenum due to the change in flow direction by 90°, respectively. The values of these components, i.e. ΔP_{ip} , ΔP_{sc} , ΔP_{se} and ΔP_{op} , are calculated from a procedure that was described in detail by Remsburg [16] as follows:

$$\Delta P_{ip} = K_{90} \frac{1}{2} G_p^2 v_l \quad (3)$$

$$\Delta P_{op} = K_{90} \frac{1}{2} G_p^2 v_l \quad (4)$$

$$\Delta P_{sc} = \frac{1}{2} G_{ch}^2 v_l [1 - \alpha^2 + 0.5(1 - \alpha)] \quad (5)$$

$$\Delta P_{se} = \frac{1}{2} G_{ch}^2 v_l \left[\frac{1}{\alpha^2} - 1 + (1 - \alpha)^2 \right] \quad (6)$$

where K_{90} , G_p , G_{ch} and α are the loss coefficient of the 90 degree turns, which is 1.2 as suggested by Phillips [17], the mass flux at the plenum, the channel mass flux and the area ratio, respectively. The area ratio is the minimum to maximum cross sectional area. For single-phase experiments, the average heat transfer coefficient is calculated from Eq. (7) below using a uniform wall temperature assumption, i.e. for a high thermal conductivity material:

$$\bar{h} = \frac{q_b'' W_b L_{ch}}{A_{ht} \Delta T_{LM}} \quad (7)$$

ΔT_{LM} is the log mean temperature difference. The wall temperature distribution along the channel was indeed uniform, e.g. the thermocouples along the flow direction indicated a temperature variation of only 0.82 K for 300 kg/m²s, see Section 4.1. The average Nusselt number is calculated from Eq. (8).

$$\overline{Nu} = \frac{\bar{h} D_h}{k_l} \quad (8)$$

The base heat flux is estimated from the calculated vertical temperature gradient at the wall using Eq. (9), while the wall heat flux is calculated from Eq. (10).

$$q_b'' = k_{cu} \left. \frac{dT}{dy} \right|_{y=0} \quad (9)$$

$$q_w'' = \frac{q_b'' A_b}{A_{ht}} \quad (10)$$

where A_b and A_{ht} are the heat sink base area and the heat transfer area, respectively. Eq. (11) is used to calculate the heat transfer area. The use of this area assumes uniform heat flux in the transverse and axial direction with three-sides heated. The input power, i.e. the power supplied to the cartridge heaters, was measured using a power meter (Hameg HM8115-2) with accuracy of $\pm 0.4\%$. The cover plate is assumed to be adiabatic during the experiments.

$$A_{ht} = (2H_{ch} + W_{ch}) L_{ch} N \quad (11)$$

During the flow boiling experiments, the local single and two-phase heat transfer coefficient are found from Eq. (12) and (13), respectively.

$$h_{sp(z)} = \frac{q_b'' (W_{ch} + W_{fin})}{(T_{wi(z)} - T_{f(z)}) (W_{ch} + 2\eta H_{ch})} \quad (12)$$

$$h_{tp(z)} = \frac{q_b'' (W_{ch} + W_{fin})}{(T_{wi(z)} - T_{sat(z)}) (W_{ch} + 2\eta H_{ch})} \quad (13)$$

The local internal surface temperature $T_{wi(z)}$ can be found from Eq. (14), while the local fluid temperature $T_{f(z)}$ can be calculated from Eq. (15).

$$T_{wi(z)} = T_{th(z)} - \frac{q_b'' b}{k_{cu}} \quad (14)$$

$$T_{f(z)} = T_{fi} + \frac{q_b'' W_b z}{\dot{m} c_{p_l}} \quad (15)$$

In the above, the local thermocouple temperature $T_{th(z)}$ is measured at each location, see Fig. 3(b), while b is the vertical distance between the channel bottom and the thermocouple (4.15 mm). The fin efficiency η and the fin parameter m can be found from Eq. (16) and (17), respectively.

$$\eta = \frac{\tanh(mH_{ch})}{mH_{ch}} \quad (16)$$

$$m = \sqrt{\frac{2h(z)}{k_{cu} W_{fin}}} \quad (17)$$

The local saturation temperature $T_{sat(z)}$ is found from the corresponding local pressure in the saturated region, see Eq. (18), by assuming a linear pressure drop with axial length. This assumption is necessary since it is difficult to insert pressure sensors inside these tiny channels without disturbing the flow.

$$P_{sat(z)} = P_{sat(z,sub)} - \left(\frac{z-L_{sub}}{L_{ch}-L_{sub}} \right) \Delta P_{tp} \quad (18)$$

In this analysis, the channel is divided into two regions; the single-phase (subcooled region) and the two-phase region. The length of the single-phase region is calculated from the following equation:

$$L_{sub} = \frac{\dot{m} c_{p_l} (T_{sat(z,sub)} - T_{fi})}{q_b'' W_b} \quad (19)$$

The local saturation pressure at the subcooled region $P_{sat(z,sub)}$ is calculated from Eq. (20) below.

$$P_{sat(z,sub)} = P_i - \frac{2fG_{ch}^2 L_{sub}}{\rho_l D_h} \quad (20)$$

The second term in the right hand side of Eq. (20) is the single-phase pressure drop, ΔP_{sp} . The local saturation temperature of the fluid at the end of the single-phase region $T_{sat(z,sub)}$ is found from this pressure. Therefore, an iteration process should be conducted between Eq. (19) and (20) to determine this length. Following from that, the two-phase pressure drop ΔP_{tp} along the channel can be found from Eq. (21).

$$\Delta P_{tp} = \Delta P_{ch} - \Delta P_{sp} \quad (21)$$

The friction factor f in Eq. (20) is calculated from Eq. (22) for developing laminar flow and Eq. (24) for fully developed flow as proposed by Shah and London [18].

$$f_{app} = \frac{3.44}{Re\sqrt{L^*}} + \frac{f_{FD} Re + \frac{K_\infty}{4L^*} - 3.44/\sqrt{L^*}}{Re(1+C(L^*)^{-2})} \quad (22)$$

$$L^* = L_{sub}/ReD_h \quad (23)$$

$$f_{FD} Re = 24(1 - 1.355\beta + 1.946\beta^2 - 1.7012\beta^3 + 0.9564\beta^4 - 0.2537\beta^5) \quad (24)$$

where β , K_∞ , C and L^* are the channel aspect ratio, the dimensionless incremental pressure drop number, the dimensionless correction factor and the dimensionless length, respectively. The values of K_∞ and C

are found based on the channel aspect ratio as proposed by Shah and London [18]. These values are 1.28 and 0.00021, respectively. The local vapour quality $x_{(z)}$ can be calculated as follows:

$$x_{(z)} = \frac{i_{(z)} - i_{l(z)}}{i_{lg(z)}} \quad (25)$$

In the above equation, the local specific enthalpy $i_{(z)}$ is given as:

$$i_{(z)} = i_i + \frac{q_b W_b z}{\dot{m}} \quad (26)$$

The average heat transfer coefficient is calculated from Eq. (27).

$$\bar{h} = \frac{1}{L_{ch}} \int_0^{L_{ch}} h_{(z)} dz \quad (27)$$

In this paper, the experimental flow patterns maps are presented using two coordinates; the vapour and liquid superficial velocities which are defined in Eq. (28) and (29) below.

$$J_{g(z)} = \frac{G_{ch} x_{(z)}}{\rho_{g(z)}} \quad (28)$$

$$J_{l(z)} = \frac{G_{ch}(1-x_{(z)})}{\rho_{l(z)}} \quad (29)$$

In this study, all thermophysical properties of HFE-7100 and calculations were conducted using the EES software. It is known that, under ambient condition, this coolant contains 53% of air by volume, i.e. a concentration of about 366 ppm, Hsu et al. [14]. This dissolved air can affect the thermal performance in micro scale heat sinks. Chen and Garimella [19] showed that degassing the dielectric coolant has a strong impact on the pressure drop and heat transfer coefficient. Therefore, a degassing process was conducted before starting the experiments to ensure that pure coolant was circulated in the rig, for more details see Al-Zaidi et al. [15]. The experimental uncertainties for all variables are summarized in Table 3. The uncertainty in the derived variables was calculated using the procedure given by Coleman and Steele [20]. The flow boiling experiments were conducted at a system pressure of 1 bar, inlet sub-cooling of 5 K, mass flux ranging from 50 to 250 kg/m²s and wall heat flux of 12.4–191.6 kW/m². The range of dimensionless parameters covered in the present study is: $Bd \approx 0.21$, $0.55 \times 10^{-3} < Bo < 9.76 \times 10^{-3}$, $40 < Re < 200$ and $0.067 < We < 1.7$.

4. Results and discussions

4.1 Temperature distribution and heat flux

As mentioned above, twelve thermocouples were inserted in the heat sink block to measure and check the temperature distribution during the experiments. An essential step is to check the temperature distribution in the vertical direction to validate the 1D heat conduction assumption adopted in the data reduction section. This included both single and two-phase flow experiments. In single-phase experiments, the uniform wall temperature method (UWT) was used to determine the average heat transfer coefficient as presented in the data reduction section. This was confirmed by presenting Fig. 4(a), which illustrates the temperature distribution at three axial locations, i.e. the first row of

thermocouples, at input power of 20 W, inlet fluid temperature of 30 °C and two different mass fluxes. As seen in this figure, the temperature variations in the axial direction was very small with the temperature difference being only 0.82 K for 300 kg/m²s and 0.5 K for 700 kg/m²s in this example. Fig. 4(b) presents the temperature distribution at six locations underneath the channels at a distance of 4.15 mm, i.e. three thermocouples at the mid plane and the other three thermocouples at the side plane. This figure was plotted for two-phase flow at input power of 80 W, inlet fluid temperature of 54.5 °C and mass flux of 200 kg/m²s. The results clearly demonstrate that the temperature distribution was uniform in the transverse direction, i.e. the heat transfer coefficient in the mid channels is nearly similar to that in the side channels. This might also indicate the uniformity of flow distribution with the present design. In multi-channel configurations, heat flux can be defined using the total channel surface area A_{ht} (wall heat flux) or the heat sink base area A_b (base heat flux), see Fig. 1. The single/two-phase heat transfer coefficient calculations and the assessment of existing correlations were based on the wall heat flux. The heat flux in the vertical direction was estimated from the vertical temperature gradient based on the assumption of 1D heat conduction (see Eq. 9). Five vertical thermocouples were plotted against the vertical distance from the bottom of the channels and a best-fit linear equation was obtained. As an example, Fig. 4(c) presents the two-phase flow results for an input power by the cartridge heaters of 130.5 W, inlet fluid temperature of 54 °C and mass flux of 250 kg/m²s. This figure shows that the vertical temperature gradient was almost linear and thus there was negligible heat loss in the transverse directions. In this case, the heat transfer rate was 129.91 W, i.e. the present heat loss was 0.45%. This and the above discussion validate the assumption of 1D heat conduction and minimal heat losses in the transverse and axial direction of the channels.

4.2 Single-phase validation

Single-phase validation was first carried out before conducting boiling experiments to ensure that all instruments work properly and within reasonable accuracy. Both of adiabatic and diabatic experiments were conducted at a system pressure near 1 bar and different mass fluxes. Fig. 5(a) shows the experimentally determined Fanning friction factor versus Reynolds number compared with the correlations given by Shah and London [18], which were proposed for laminar developing and fully developed flow in horizontal non-circular channels, see Appendix I. It can be seen from this figure that there was a good agreement between the experimental results and the correlation for fully developed flow with a mean absolute error (MAE) of 22.1%. The average Nusselt number versus Reynolds number was plotted and compared with three existing correlations (see Appendix I) as shown in Fig. 5(b). Stephan and Preuber [21] proposed a correlation for laminar developing flow in a single passage. Jiang et al. [22] proposed two correlations for laminar flow in uniformly heated microchannel heat exchangers based on the dimensionless length (L^*), i.e. one correlation for $L^* < 0.05$ and another for $L^* > 0.05$, see Appendix I. Mirmanto [23] proposed a correlation for laminar developing water flow in a horizontal single rectangular microchannel with three-sides heated. The correlation by Stephan and Preuber [21]

predicted the results well with a MAE of 22.7%, while the correlation by Jiang et al. [22] showed poor prediction with a MAE of 30.2%. The correlation by Mirmanto [23] predicted the experimental data very well with a MAE of 9.8%. The present heat sink has an adiabatic cover plate and heated from the bottom side, similar to the single channel experiments of [23]. The single-phase results described above demonstrate that the measurement system and calibration can provide accurate results for the flow boiling experiments.

4.3 Flow boiling patterns

The effect of heat and mass flux on flow patterns is presented and discussed in this section. Flow visualization was conducted along the mid plane of the heat sink at three different locations; near the channel inlet, middle and outlet. The results showed that the main regimes were bubbly, slug, churn and annular flow as shown in Fig. 6, for mass flux of $50 \text{ kg/m}^2\text{s}$. Confined bubbly flow, identified by bubbles of round ends that filled the channel cross section, was also seen for a short period of time as presented later in Fig. 7. Figs. 6(a-c) show the bubbly, slug and annular flows observed along the channel at wall heat flux of 29.2 kW/m^2 , while Fig. 6(d) shows the observed churn flow at wall heat flux of 36 kW/m^2 . Bubbly flow was seen near the channel inlet and the onset of nucleate boiling occurred at the channel corners. Numerous small nucleating bubbles were observed at these locations and the size of these bubbles was smaller than the channel width. Bubble generation at the channel corners was also observed by other researchers, such as [24-26], with the corners behaving as nucleation sites, [27,28]. As seen in the figure, in bubbly flow near the channel inlet, the channel bottom surface was still not active. Fig. 7 shows a sequence of pictures for bubble nucleation near the channel inlet during a 70 ms period to clarify the bubble growth and coalescence to form confined bubble, elongated bubble and slug flow. At an arbitrary time of 0 ms, a new nucleation site can be identified at the channel corner, see red circle. After 2 ms, the nucleating bubble can be clearly seen at this location. The bubble departed the nucleation site, slid along the channel wall and continued to grow due to evaporation and coalescence with other small bubbles in the time interval 2–50 ms. After 60 ms, the bubble grew and filled the channel cross section resulting in the formation of confined bubble, which did not sustain for long period. Once the bubble touched the channel sidewalls, a bidirectional sudden expansion in bubble size, in the downstream and upstream directions, was observed as shown at time of 65 ms. This sudden expansion in size is probably due to additional high heat transfer rates through the sidewalls. This is also responsible for flow reversal and instability, see Section 4.6 below. At time of 70 ms, a vapour slug occurred followed by small bubbles. Slug flow was observed near the channel middle as shown in Fig. 6(b). When the vapour slug velocity became higher, due to the increase in evaporation rate along the channel, the slug shape was distorted and changed into churn flow, see Fig. 6(d). At the channel outlet, annular flow with a vapour core surrounded by a liquid film was observed as shown in Fig. 6(c). The progress of flow regimes structure observed in this study is shown schematically in Fig. 8.

The effect of heat flux on the flow pattern features is illustrated in Fig. 9 and 10. As seen in Fig. 9 for mass flux of $50 \text{ kg/m}^2\text{s}$, more nucleation sites were activated at channel corners and bottom surface when the wall heat flux increased from 29.2 to 58.1 kW/m^2 . For low heat flux, few active nucleation sites were observed only at the channel corners. Moreover, the bubble size was larger at high heat flux compared to that observed at low heat flux. Fig. 10 presents the features of flow patterns at mass flux of $150 \text{ kg/m}^2\text{s}$ and three different wall heat fluxes. The flow patterns in this figure were captured near the channel middle. When the heat flux was set at 30.4 kW/m^2 , bubbly flow was observed, while slug flow occurred at a heat flux of 58.3 kW/m^2 . When the heat flux increased more, i.e. 113.1 kW/m^2 , the flow pattern changed to churn flow. The vapour quality increases with increasing heat flux and this can result in different flow patterns at specified location.

Fig. 11 shows some interesting features with the increase of heat flux for a mass flux of $100 \text{ kg/m}^2\text{s}$. At low heat flux, i.e. 23.7 kW/m^2 , slug flow was observed near the channel middle as shown in Fig. 11(a). When the heat flux increased to 46.5 kW/m^2 , slug flow was still observed but with small nucleating bubble in the liquid film at the channel sidewalls as shown in Fig. 11(b). Similar features, i.e. nucleating bubbles in the liquid film, were visualised in annular flow when the heat flux increased to 57.8 kW/m^2 , see Fig. 11(c). These bubbles could be suppressed towards the channel outlet, especially when the liquid film becomes too thin. At low heat flux, the wall superheat was low and consequently nucleation may be suppressed. With increasing heat flux, the wall superheat increases and may become sufficient for the activation of these nucleation sites. Small nucleating bubbles in the liquid film of annular flow were also reported by other researchers, such as Harirchian and Garimella [29] and Borhani and Thome [30] using dielectric refrigerants, such as FC-77 and R245fa, respectively, in horizontal rectangular multi-microchannels.

Fig. 12 shows the effect of mass flux on flow patterns captured at the channel middle for a wall heat flux of 25 kW/m^2 . At the lowest mass flux, i.e. $G = 50 \text{ kg/m}^2\text{s}$, the flow pattern was slug flow. When the mass flux increased to $250 \text{ kg/m}^2\text{s}$, the flow pattern became bubbly flow. This is due to the fact that, for a fixed wall heat flux, the vapour quality decreases with increasing mass flux, resulting in different flow patterns.

4.4 Comparison with existing maps

The experimental flow patterns map was presented in Fig. 13 using two coordinates; the vapour and liquid superficial velocities. This map was plotted at a system pressure of 1 bar, wall heat flux ranging from 12.4 to 191.6 kW/m^2 and mass flux of 50 – $250 \text{ kg/m}^2\text{s}$. It is worth mentioning that, this map was plotted based on the local vapour quality (local superficial velocities) and the flow patterns captured at the three locations, i.e. near inlet, middle and outlet. It is obvious that, bubbly flow occurred at vapour superficial velocity nearly less than 1 m/s . Other flow patterns occurred, i.e. slug, churn and annular flow with increasing vapour superficial velocity due to the increase of vapour quality along the

channels. In the present study, three existing flow pattern maps were compared with the experimental data. These maps were chosen because they were proposed for horizontal non-circular microchannels.

4.4.1 Comparison with Akbar et al.[31]

This map was proposed based on the experimental data for horizontal and vertical circular and semi-triangular channels. Air-water was tested as the working fluid in a diameter ranging from 0.866 to 1.6 mm. The authors presented their map using the Weber number coordinates that included four regions as follows:

1. Surface tension dominated region: Bubbly, slug and plug flow.

$$We_{gs} \leq 0.11We_l^{0.315} \quad \text{For } We_{ls} \leq 3 \quad (30)$$

$$We_{gs} \leq 1 \quad \text{For } We_{ls} > 3 \quad (31)$$

2. Inertia dominated region I: Annular and wavy annular flow.

$$We_{gs} \geq 11We_l^{0.14} \quad We_{ls} \leq 3 \quad (32)$$

3. Inertia dominated region II: Dispersed flow.

$$We_{gs} > 1 \quad We_{ls} > 3 \quad (33)$$

4. Transition region, churn flow is included in this region.

Fig. 14 shows the comparison with Akbar et al. [31] map and demonstrates that most of the data points of bubbly and annular flow are well predicted. The map predicted poorly the data of slug flow. It is obvious from their map that most of the data for churn flow was predicted well, i.e. within the transition region.

4.4.2 Comparison with Harirchian and Garimella [32]

Several flow boiling experiments were conducted by the authors [32] using FC-77 at a heat flux range from 25 to 380 kW/m² and mass flux of 225–1420 kg/m²s. Twelve heat sinks with a hydraulic diameter ranging from 0.096 to 0.707 mm were manufactured. Each heat sink was made of silicon and consisted of horizontal multi-microchannels. The authors proposed a new dimensionless number, convective-confinement number ($Bd^{0.5}Re$), to present their map. Moreover, they classified their map into two groups; confined and unconfined. The confinement effect dominated when the channel cross-sectional area was occupied by the vapour phase with uniform liquid film. Their map was plotted using two coordinates, namely the convective-confinement number and the dimensionless heat flux ($BoRe$) as shown in Fig. 15. The following equations were used to define the transition boundaries in their map.

$$Bd^{0.5}Re = 160 \quad (34)$$

$$Bo = 0.017(Bd^{0.4}Re^{-0.3}) \quad (35)$$

It is obvious from Fig. 15 that all the data points of bubbly flow were poorly predicted by their map, while only few points of slug flow were located in the confined slug region. In contrast, all the data points of both churn and annular flow were in the right area indicated by this map.

4.4.3 Comparison with Costa-Patry and Thome [33]

This map was proposed for horizontal single tubes and rectangular multi-microchannels with hydraulic diameter ranging from 0.146 to 3.04 mm. The data used to develop this map included four fluids namely; R134a, R236fa, R245fa and R1234ze(E) at heat flux of 8–260 kW/m² and mass flux of 100–1100 kg/m²s. The authors [33] found that, for each heat flux, the local heat transfer coefficient decreased to a minimum value then increased again, i.e. the trend of the local heat transfer coefficient versus quality is like a V-shape. They reported that this minimum value corresponded to the transition from coalescing bubble regime to annular regime. Accordingly, they proposed a transition criterion from coalescing bubble regime (CB) to annular regime (A), based on the Boiling number and the Confinement number, see Eq. (36). They also recommended the flow pattern map by Ong and Thome [34] for other transition criteria. The transition boundary from isolated bubble regime (IB) to coalescing bubble regime (CB) can be defined using Eq. (37) (Ong and Thome [34]).

$$x_{CB/A} = 425 \left(\frac{\rho_g}{\rho_l} \right)^{0.1} \left(\frac{Bo^{1.1}}{Co^{0.5}} \right) \quad (36)$$

$$x_{IB/CB} = 0.36 Co^{0.2} \left(\frac{\mu_g}{\mu_l} \right)^{0.65} \left(\frac{\rho_g}{\rho_l} \right)^{0.9} \left(\frac{GD_h}{\mu_g} \right)^{0.75} Bo^{0.25} We_l^{-0.91} \quad (37)$$

According to Ong and Thome [34], the isolated bubble regime included bubbly and slug-plug flow, while the coalescing bubble regime represented slug, churn and semi-annular flow. Both wavy-annular and smooth-annular flows were included in the annular regime. Their map was compared with the present experimental data as shown in Fig. 16. It indicates that most of the experimental data of bubbly and slug flow were located within the predicted regions. However, at $G \geq 150$ kg/m²s, some data points of slug flow were located into the annular regime. All the data points of annular flow were predicted very well by this map. Contrary to that, most of the data of churn flow were poorly predicted, i.e. these data fall into the annular regime.

4.5 Two-phase heat transfer

Several experiments were performed to study the effect of local vapour quality, heat flux and mass flux on the thermal performance of the present heat sink. Table 4 presents the operating conditions at a system pressure of 1 bar, inlet sub-cooling near 5 K, base heat flux of 21.7–335.3 kW/m² and mass flux ranging from 50 to 250 kg/m²s. The local heat transfer coefficient was calculated at three locations using data from the three thermocouples embedded in the copper block along the axial direction and 10 mm apart, see Fig. 3(b) and Section 3.

Fig. 17 depicts the effect of mass flux on the conventional boiling curve plotted as base heat flux versus wall superheat. The present data were obtained at exit vapour quality near 0.9. Hence, this figure provides the maximum design limit for flow boiling applications, i.e. the maximum base heat flux at these operating conditions. Boiling commenced smoothly at wall superheat of 2–3.7 K; then the heat

flux increased with wall superheat reaching a maximum base heat flux value of 335.3 kW/m² at wall superheat of 16.4 K, i.e. surface temperature of 76.4 °C. This figure also shows that there was no clear effect of mass flux on the boiling curve. This finding was also reported by Mirmanto [23], Soupremanien et al. [25], Fayyadh et al. [26] and Bertsch et al. [35].

Fig. 18 shows the local heat transfer coefficient versus local quality at mass flux of 250 kg/m²s and different wall heat fluxes. As seen in this figure, the peak value of the local two-phase heat transfer coefficient occurred at vapour qualities slightly above zero, i.e. at boiling incipience when the flow regime was bubbly flow. This could be due to the evaporation in the liquid micro-layer underneath the nucleating bubbles. Subsequently, the local heat transfer coefficient decreased with increasing local vapour quality, i.e. in the slug, churn and annular flow regimes. This reduction in the heat transfer coefficient with vapour quality could be attributed to the following possible reasons: (i) for low and moderate heat fluxes, the reason could be the reduction in local pressure along the channel and consequently the reduction in saturation temperature. As mentioned above, the local saturation temperature was obtained in the present study based on a linear pressure drop assumption. Fig. 19 illustrates the local saturation temperature obtained from the corresponding local pressure and wall temperature along the channel at different wall heat fluxes. In real flow boiling systems, the assumption of linear pressure drop variation may not be valid especially in the very low quality region, i.e. around boiling incipience, as discussed by Mahmoud and Karayiannis [36]. Huang and Thome [37] proposed a pressure drop model based on the separated flow model assumption and the correlation by Zivi [38] for void fraction. They used their model to predict the local pressure along the channel and reported that the local pressure decreased according to a parabolic curve rather than a linear curve. At boiling incipience, the local pressure based on the linear assumption was found to be much higher than that based on the model predictions. Accordingly, low local pressure results in low local saturation temperature and thus high wall superheat (low local heat transfer coefficient). In other words, the local heat transfer coefficient at boiling incipience will be higher in the case of a linear pressure drop assumption. It is worth mentioning that, the parabolic variation of pressure drop along the channel reported by [37] was only based on a model rather than direct measurements, which is still very challenging in microchannels. (ii) At high heat fluxes, the reason could be the combined effect of the reduction in local pressure and increase in wall temperature along the channel. This figure shows that the local saturation temperature decreased continuously and there was a noticeable increase in the local wall temperature especially at high heat fluxes. This may be due to the local dry patches that can lead to an increase in the local wall temperature towards the channel exit. As a result, the difference between the local wall temperature and saturation temperature (wall superheat) increased towards the channel outlet and thus the local heat transfer coefficient could decrease. It is worth mentioning that, the axial wall temperature variation was within ± 1.5 K on the heat sink at maximum wall heat flux, 191.6 kW/m², while this variation became smaller with decreasing heat flux. The reduction in heat transfer coefficient with increasing quality was also reported by [39-41]. All the above points require further investigation.

Fig. 18 also shows the effect of wall heat flux on the local heat transfer coefficient. It can be seen that the local heat transfer coefficient increased, when the heat flux increased from 25.12 to 191.6 kW/m², which agrees with Lazarek and Black [42], Bao et al. [43], Sobierska et al. [44] and Fayyadh et al. [26]. The figure was divided into two regions, with respect to local vapour quality, namely low and intermediate/high vapour quality regions, in order to clarify this effect. In the low vapour quality region ($x < 0.1$), where the flow pattern was bubbly flow, increase of heat flux led to an increase in the number of active nucleation sites on the channel surface, see Section 4.3. As a consequence, the heat transfer coefficient increased. In the intermediate/high vapour quality region ($x > 0.1$), where the flow pattern was slug or annular flow, the increase in the liquid film evaporation rate could be the reason for increasing the heat transfer coefficient with heat flux, at low heat fluxes. At moderate to high heat fluxes, there is a possibility for the contribution of both liquid film evaporation and nucleation in the liquid film as the heat flux increased, see figure 11.

Fig. 20 shows the effect of mass flux on the local heat transfer coefficient plotted versus local vapour quality for wall heat flux of 57.8 kW/m². This figure demonstrates that the effect of mass flux was negligible. This insignificant mass flux effect was also reported by other researchers, such as [43] and [45-48]. Fig. 21 shows the effect of wall heat and mass fluxes on the average heat transfer coefficient and indicates insignificant mass flux effect with strong heat flux effect. It can be concluded from the previous results that, the local two-phase heat transfer coefficient increases with wall heat flux, while it decreases moderately with increasing local vapour quality. Moreover, there is an insignificant mass flux effect at this scale and with this particular fluid.

4.6 Flow reversal and instability

Flow reversal and boiling instability are very common in multi-microchannel configurations. Flow reversal in micro scale evaporators can cause high pressure drop fluctuations and deterioration of flow distribution as mentioned by Tuo and Hrnjak [49]. Flow reversal was also reported by Chen and Garimella [50], Yang et al. [9] and Fayyadh et al. [26]. These experimental studies were conducted using different refrigerants in horizontal multi-microchannel configurations. Consolini and Thome [51] investigated experimentally the effect of stable and unstable flow on the flow boiling heat transfer data using three different refrigerants; R134a, R236fa and R245fa. In their study, two horizontal stainless steel microchannels with inner diameter of 0.51 and 0.79 mm were manufactured. They conducted their experiments at heat flux up to 200 kW/m² and mass flux ranging from 300 to 2000 kg/m²s. Their results showed that the trend of local heat transfer coefficient versus vapour quality changed significantly when the flow was stable or unstable. For example, the local heat transfer coefficient for R245fa increased with vapour quality, when the flow was stable. However, the local heat transfer coefficient did not change with quality, when the flow was unstable, i.e. high amplitude instability. Moreover, higher heat transfer coefficient was found for stable flow compared to that for unstable flow. Similar trend was also found for R236fa. In contrast, for refrigerant R134a, the heat transfer coefficient for stable flow was

identical to that for unstable flow. The insensitivity of R134a to the flow instabilities makes it as a good refrigerant for cooling electronic components as they mentioned.

In this study, flow reversal occurred due to the rapid bubble growth near the channel inlet and slug formation, i.e. transition from confined bubble to slug, as presented previously in Fig. 7; Section 4.3. It becomes more pronounced at high heat fluxes and low mass fluxes. In the present study, flow reversal was observed for all mass fluxes. The recorded signals were analysed to assess whether the flow reversal observed in the present study affects system parameters (pressure, pressure drop, temperature). Fig. 22 depicts the measured pressure drop signal for mass flux of $250 \text{ kg/m}^2\text{s}$ at different wall heat fluxes. It is clear from this figure that, the measured pressure drop and amplitude of oscillations increased with increasing heat flux. For instance, at the lowest wall heat flux, i.e. 15.1 kW/m^2 , liquid flow was observed and the measured pressure drop (mean value) was 0.27 kPa . It is obvious that, before boiling incipience, the system was very stable with amplitude fluctuation (the difference between the peak and the mean value) of 0.044 kPa . When the wall heat flux increased to 25.12 kW/m^2 , flow boiling occurred and thus high oscillations in the pressure drop signal were measured with amplitude fluctuation of 0.18 kPa . The pressure drop was measured as 0.46 kPa . With further increase in heat flux, i.e. 191.6 kW/m^2 , this fluctuation increased up to 0.65 kPa at measured pressure drop of 4 kPa . A Fast Fourier Transform analysis was conducted on the measured pressure drop data to clarify the frequency distribution and amplitude for different heat fluxes. The result of this analysis is presented in Fig. 23 and shows that the frequency of oscillation and amplitude increased with increasing heat flux at constant mass flux. For example, at low heat flux, the dominant frequency of the pressure drop reached 3.42 Hz at maximum amplitude of 0.027 . At high heat flux, this frequency became higher, i.e. 4.15 Hz , at amplitude of 0.103 . In other words, the high frequency of the pressure drop values could mean more intense flow instability. Although flow reversal occurred in this study, the flow boiling heat transfer results were not affected. This is inferred from the measured signals of pressure drop, inlet/outlet pressure, inlet/outlet fluid temperature and thermocouple temperature along the channels, which did not fluctuate significantly during the present experiments. Figs. 22 and 24 depict these signals at the maximum heat and mass flux. It can be seen that the maximum deviation from the mean value was 8.15% for the measured pressure drop, 0.81% for the inlet pressure, 0.68% for the outlet pressure, 0.37% for the inlet fluid temperature, 0.04% for the outlet fluid temperature and between 0.11% to 0.33% for the wall thermocouples. Consolini and Thome [51] also found that the heat transfer results for R134a were not affected by flow instability, although the results of R236fa and R245fa showed significant effect. Therefore, further work is needed to clarify the effect of flow instability on the heat transfer results, which could include fluid dependency.

4.7 Evaluation of existing heat transfer correlations

The accuracy of two-phase heat transfer correlations is an important consideration in thermal design of miniature cooling systems. Fifteen existing two-phase heat transfer correlations were selected and

compared with the experimental results. These correlations were proposed for horizontal/vertical flows, conventional and mini/microchannels, circular/non-circular channels and single and multi-channels. The percentage of data points predicted within $\pm 30\%$ error bands (Θ) and the mean absolute error (MAE) were used to evaluate these correlations as follows:

$$\Theta = \frac{N_{pred}}{N_{exp}} 100\% \quad (38)$$

$$MAE = \frac{1}{N} \sum \left| \frac{h_{pred} - h_{exp}}{h_{exp}} \right| 100\% \quad (39)$$

where N is the number of data points. It is worth mentioning that, some of these correlations were proposed for fully heated channel, i.e. all sides heated, while the present multi-microchannels are heated from the bottom side with an adiabatic cover plate. Therefore, a correction factor should be used to adjust the values of these correlations for a partly heated channel as presented in Eq. (40). This was also adopted by other researchers, such as [39], [52] and [53].

$$HTC = \left(\frac{Nu_3}{Nu_4} \right) h_{tp} \quad (40)$$

where HTC , h_{tp} , Nu_3 and Nu_4 are the adjusted two-phase heat transfer coefficient, the two-phase heat transfer coefficient calculated from the correlation, Nusselt number for thermally developed laminar flow with three-sides and four-sides heated transfer, respectively. The last two parameters are calculated from Eq. (41) and (42) as proposed by [18].

$$Nu_3 = 8.235(1 - 1.833\beta + 3.767\beta^2 - 5.814\beta^3 + 5.361\beta^4 - 2\beta^5) \quad (41)$$

$$Nu_4 = 8.235(1 - 2.042\beta + 3.085\beta^2 - 2.477\beta^3 + 1.058\beta^4 - 0.186\beta^5) \quad (42)$$

Appendix IIa presents the details and applicability range of each correlation, while Fig. 25 illustrates the results of this comparison. Shah [54], Kandlikar [55] and Liu and Winterton [56] proposed correlations for conventional channels but are included here since they predicted the results fairly well. Shah [54] selected the larger value of the heat transfer coefficient in the nucleate and convective boiling. He defined the nucleate boiling component (E) as a function of the Boiling number (Bo), while the convective boiling component (S) was described as a function of the Convection number (N_{co}). This correlation predicted 65.71% of the present data with a MAE of 24.64%. Kandlikar [55] used the same approach, for calculating the total heat transfer coefficient. He selected the larger value of the heat transfer coefficient in nucleate and convective boiling. Both the Boiling number (Bo) and the Convection number (N_{co}) were proposed in his correlation. The comparison indicated that, 62.3% of the data were predicted with a MAE of 26.1%. Liu and Winterton [56] correlated the nucleate boiling component using the pool boiling correlation given by Cooper [57]. They combined the nucleate and convective contributions using the asymptotic approach with a power of 2. Their correlation predicted 76.57% of the data with a MAE of 20.57%.

The following discussion refers to correlations developed for small to micro passages. Lazarek and Black [42] conducted an experimental investigation of flow boiling heat transfer of R113 in vertical

stainless steel tubes with inner diameter of 3.1 mm and reported that nucleate boiling was the dominant heat transfer mechanism. They correlated the heat transfer coefficient in terms of dimensionless numbers, i.e. Nusselt, Reynolds and Boiling number. This correlation predicted only 44.57% of present data with a MAE of 36.01%. Warriar et al. [58] carried out an experimental investigation of flow boiling of FC-84 in horizontal rectangular multi-microchannels. The heat sink was made of aluminum and had five parallel channels with hydraulic diameter of 0.75 mm. They included the Boiling number, vapour quality and the single-phase heat transfer coefficient in their new correlation. In comparison with the present data, their correlation predicted only 38.3% of the present experimental data with a MAE of 48.32%. Lee and Mudawar [59] carried out an experimental study of flow boiling heat transfer using two fluids, namely water and R134a in horizontal parallel rectangular microchannels. These channels were made of oxygen-free copper with a hydraulic diameter of 0.348 mm. Three correlations were proposed according to the vapour quality ranges, i.e. $x < 0.05$, $0.05 < x < 0.55$ and $x > 0.55$. They found that, at vapour quality less than 0.05, the nucleate boiling was the dominant mechanism, while the convective boiling dominated at moderate and high qualities. They correlated the heat transfer coefficient as a function of liquid Weber number, Boiling number, Martinelli parameter and single-phase heat transfer coefficient, which was calculated using laminar or turbulent vapour flow as shown in Appendix IIa. The comparison with their correlation resulted in a significant scatter with a MAE of 60.06%. Sun and Mishima [60] collected flow boiling data that included 2505 data points for eleven different fluids, vertical and horizontal flows and hydraulic diameter ranging from 0.21 to 6.05 mm. The heat flux ranged from 5 to 109 kW/m² and the mass flux from 44 to 1500 kg/m²s. They reported that the correlation by Lazarek and Black [42] predicted the data very well. Therefore, they proposed a correlation by modifying the correlation of Lazarek and Black [42]. They included the liquid Weber number, which represents the convective boiling component. This correlation did not predict our results, i.e. Θ of 0.00%, with a MAE of 54.41%. A large number of flow boiling databases were collected by Li and Wu [61] including different fluids, vertical and horizontal flows at a hydraulic diameter ranging from 0.16 to 3.1 mm. They proposed a flow boiling heat transfer correlation, based on more than 3700 data points, as a function of the superficial liquid Reynolds number, Boiling number and Bond number. The last dimensionless parameter was used to consider the effect of surface tension. Their correlation predicted 67.43% of the present data with a MAE of 23.16%. A universal correlation was proposed by Kim and Mudawar [62] based on 37 sources including 18 working fluids, vertical and horizontal flows and single and multi-channels with a hydraulic diameter of 0.19–6.5 mm. Their data included heat flux ranging from 5 to 109 kW/m² and mass flux from 19 to 1608 kg/m²s. The heat transfer coefficient was based on both nucleate and convective boiling. When their correlation was compared with the present experimental data, 22.3% of the data was predicted with a MAE of 40.51%. Mahmoud and Karayiannis [36] proposed an empirical correlation for flow boiling of R134a in vertical stainless steel micro tubes ranging from 0.52 to 4.26 mm. Their correlation was developed based on 5152 data points including heat flux of 1.7–158 kW/m² and mass flux ranging from 100 to 700 kg/m²s. They proposed a new

experimental enhancement factor (F) according to the approach used by Chen [63]. As seen in Fig. 25, this correlation was able to predict 72.57% of the data with a MAE of 21.04%. Although their correlation was proposed for vertical channels, it showed a good agreement with horizontal channels. This was also reported by Sempertegui-Tapia and Ribatski [64]. They compared 3409 flow boiling data points including four fluids; R134a, R1234ze(E), R1234yf and R600a, in a horizontal circular channel with diameter of 1.1 mm. The correlation by [36] predicted their data with a MAE ranging from 22.3% to 29.2%. This correlation was also in a good agreement when compared with the results of R134a in horizontal rectangular multi-microchannels reported by Fayyadh et al. [26] with a MAE of 19%. Li and Jia [65] conducted an experimental study of flow boiling of R134a in three-sides heated multi-microchannels with a hydraulic diameter of 0.5 mm. Their experiments were conducted at heat flux values up to 802.12 kW/m² and mass flux ranging from 373.3 to 1244.4 kg/m²s. They divided their results into three regimes, namely I, II and III. Regime I was nucleate boiling when the heat transfer coefficient increased with heat flux for all mass fluxes. A small effect of mass flux was found in this regime. However, a slight reduction in the heat transfer coefficient with heat flux, at high heat fluxes, was reported. Regime II was identified as convective boiling when the mass flux had a significant effect on the heat transfer coefficient. However, heat flux effect was also observed in this regime. The dry out regime, i.e. regime III, was characterised when the heat transfer coefficient decreased with heat flux for most mass fluxes. Two correlations for saturated boiling in horizontal rectangular multi-microchannels were proposed, based on these regimes. One correlation was recommended for nucleate boiling dominant regime, while the other was proposed for the convective boiling regime. Their first correlation was compared with the present data and was able to predict the current experimental results with a reasonable accuracy, i.e. 96% of data points with a MAE of 13.84%. The comparison with the second correlation was not so good, i.e. with a MAE of 51.42%. Lim et al. [47] conducted an experimental study of flow boiling heat transfer of water in a horizontal square microchannel with hydraulic diameter of 0.5 mm. They proposed a correlation based on Reynolds number, Boiling number and the liquid Froude number. Their correlation under predicted the present data, i.e. only 8% with a MAE of 61.42%. Thiangtham et al. [66] carried out an experimental investigation of flow boiling heat transfer of R134a in horizontal multi-microchannels. Twenty seven rectangular microchannels were made of oxygen-free copper with a hydraulic diameter of 0.421 mm. They proposed an empirical flow boiling heat transfer coefficient correlation as a function of dimensionless groups. This correlation under predicted the present experimental data with a MAE of 81.96%. Markal et al. [67] carried out an experimental study of flow boiling heat transfer of de-ionized water in horizontal rectangular multi-microchannels. Different aspect ratios ranging from 0.37 to 5 at constant hydraulic diameter of 0.1 mm and different hydraulic diameters of 0.1–0.25 mm at constant aspect ratio of 1 were tested. The empirical correlation proposed by the authors included several parameters such as aspect ratio, superficial liquid Reynolds number, Boiling number, vapour quality, Webber number, Prandtl number, hydraulic diameter and the fluid thermal conductivity. Their correlation under predicted the present data with a large MAE of

397.6%. Shah [68] developed a new correlation by taking into account the effect of Weber number and Boiling number. The author proposed a factor (F) to modify his correlation [54] as shown in Appendix IIa. The new correlation was verified with a large database including 31 fluids, different channel shapes, vertical and horizontal flows and fully or partly heated channel with a diameter ranging from 0.38 to 27.1 mm at mass flux ranging from 15 to 2437 kg/m²s. When this correlation was compared with the present results, 81.14% of the data points were predicted with a mean absolute error of 18.74%.

Discrepancies in experimental results were presented by Karayiannis et al. [2] explaining that the heated length and inner surface characteristics can be important parameters. Pike-Wilson and Karayiannis [69] presented research on the effect of material on the heat transfer characteristics of flow boiling of R245fa. In a recent publication, Mahmoud and Karayiannis [4] extended this work and explained in detail the dependency of the nucleation and bubble dynamics in microchannels, boiling flow patterns, heat transfer rates and pressure drop on the choice of fluid and the geometry and surface characteristics of the channels. This dependency is the result of different fluid properties, such as surface tension, latent heat and thermal conductivity, and the range of hydraulic diameter, channel aspect ratio, channel length and material and surface roughness of the channels. The effect of channel aspect ratio and geometry was discussed by Markal et al. [67] and Sempertegui-Tapia and Ribatski [70]. Channel inclination could result in different heat transfer characteristics due to the different bubble or slug velocity, buoyancy force effect, as found by Wang et al. [13]. Flow reversal and flow instability can affect the overall performance of the microchannels, see Yang et al. [9] and Consolini and Thome [51]. Mahmoud and Karayiannis [71] stated that the volume of the inlet/outlet plenum had a significant effect on the flow instability, i.e. large volume resulted in a reduction in the amplitude of the pressure drop and the inlet/outlet pressure signals.

Differences in the above as well as different experimental conditions can result in different experimental data and subsequent correlations. There is further work to be done in this area. From the above comparisons, it can be concluded that the heat transfer correlations presented by Li and Jia [65], Shah [68] and Mahmoud and Karayiannis [36] with a MAE of 13.84%, 18.74% and 21.04%, respectively, provided reasonable agreement. The correlation of Liu and Winterton [56], which included a large range of diameters (2.95 to 32 mm), predicted the data reasonably well, i.e. 76.57% of the data predicted with an MAE value of 20.57%.

4.8 Evaluation of existing pressure drop correlations

Pressure drop correlations proposed for conventional and microchannels are presented in Appendix III. Ten two-phase pressure drop correlations were compared with the present data and the results are presented in Fig. 26. Reasonable accuracy of two-phase pressure drop prediction helps to design and select the required pump in systems. It is known that, in horizontal channels, two-phase pressure drop included acceleration and frictional pressure drop components. The void fraction should be used in order to calculate the acceleration pressure drop. The Martinelli void fraction correlation was used by

Lockhart and Martinelli [72] to calculate this pressure drop, while other researchers such as Mishima and Hibiki [73], Qu and Mudawar [74], Lee and Garimella [75], Kim and Mudawar [76], Keepaiboon et al. [77], Huang and Thome [37], Li and Hibiki [78] and Markal et al. [79] used the void fraction correlation proposed by Zivi [38], which was developed for macro scale channels. However, it is used in mini or micro scale passages since there is lack of generally proposed and accepted models for these scales, Lee and Garimella [75].

Four different sources were used by Lockhart and Martinelli [72] to propose a two-phase multiplier. These sources included air/water, air/benzene, air/kerosene and air/oils in circular tubes with inner diameter ranging from 1.5 to 25.8 mm. Their two-phase multiplier was calculated according to the flow condition, i.e. laminar or turbulent flow. Their correlation over predicted the present data with a MAE of 157.6%. The Homogenous flow model was developed based on the assumption that both liquid and vapour phases were modelled as one phase and the slip velocity between them was assumed to be negligible, see Collier and Thome [80]. The two-phase friction factor was assumed to be 0.003 as recommended by Qu and Mudawar [74]. When this correlation was compared with the present data, 38.6% of the data was predicted with a MAE of 37.15%. Mishima and Hibiki [73] conducted an experimental investigation using different fluids in horizontal and vertical channels with inner diameter ranging from 1.05 to 4.08 mm. In their study, the Chisholm constant (C) was modified as a function of inner diameter to calculate the frictional pressure drop. This constant was verified based on data collected from five sources, including vertical and horizontal flow and circular and rectangular channels. They found that this constant decreased with decreasing inner diameter as shown in Appendix III. Their correlation predicted 84.21% of the total data points with a mean absolute error of 18.7%. Mahmoud et al. [81] evaluated pressure drop correlations using data for R134a and stainless steel tubes of diameter 0.5 and 1.1 mm and also reported that the correlation by Mishima and Hibiki [73] predicted their data very well. Qu and Mudawar [74] studied the hydrodynamic instability and flow boiling pressure drop of water in horizontal rectangular multi-channels with a hydraulic diameter of 0.35 mm. Their heat sink was made of copper including twenty one channels. They modified the Chisholm constant using the experimental data by incorporating the effect of mass flux and channel size. This correlation predicted 47.37% of the present experimental results with a MAE of 36.51%. Lee and Garimella [75] used water as the working fluid in horizontal rectangular multi-channels. The heat sink was made of silicon with hydraulic diameter ranging from 0.162 to 0.571 mm. They also modified the Chisholm constant as a function of mass flux and hydraulic diameter. It can be seen from this figure that their correlation over predicted the data with a MAE of 113%. Kim and Mudawar [76] proposed a new correlation based on 2378 data points collected from various sources. The data included nine different fluids, R12, R22, R134a, R245fa, R410a, FC-72, CO₂, ammonia and water, for horizontal and vertical flows. Different channel geometries were included in their data, i.e. circular and rectangular channels, with hydraulic diameter ranging from 0.349 to 5.35 mm. The comparison with the present data showed that this correlation over predicted our results with a MAE of 75.25%. Keepaiboon et al.

[77] conducted an experimental study of flow boiling pressure drop of R134a in a horizontal single rectangular microchannel with a hydraulic diameter of 0.68 mm. A new (C) coefficient in the two-phase frictional multiplier, i.e. Chisholm constant, was proposed based on their experimental data. This constant included the effect of liquid only Reynolds number, the Confinement number and the Martinelli parameter. It was found that their correlation predicted the present experimental data very well with a MAE of 19.2%. Huang and Thome [37] conducted an experimental investigation of flow boiling pressure drop using three different fluids; R1233zd(E), R245fa and R236fa in horizontal square microchannels. Silicon was used to fabricate 67 parallel channels with a hydraulic diameter of 0.1 mm. In their study, the Chisholm constant was modified including the liquid only Reynolds number and the superficial vapour Reynolds number. Their correlation was able to predict 5.26% of the data with a MAE of 96.1%. Li and Hibiki [78] proposed a correlation to calculate the two-phase frictional pressure drop based on 1029 data points obtained from eleven sources, including mini and microchannels, eight fluids with hydraulic diameter ranging from 0.109 to 2.13 mm. They divided the database into three groups; laminar liquid-laminar vapour, laminar liquid-turbulent vapour and turbulent liquid-turbulent vapour. The Chisholm constant was modified as a function of the vapour quality, the two-phase viscosity number and the two-phase Reynolds number. Their correlation predicted 35.1% of the present data with a MAE of 61.63%. Markal et al. [79] proposed two correlations for low mass fluxes based on an experimental investigation. They tested de-ionized water in horizontal rectangular multi-microchannels. Nine heat sinks made of silicon with different aspect ratios ranging from 0.37 to 5 at hydraulic diameter of 0.1–0.25 mm were used. They modified the (C) parameter in the two-phase frictional multiplier as a function of liquid only Reynolds number, aspect ratio, Boiling number, Webber number, hydraulic diameter and the two-phase length. An additional dimensionless correlation was proposed to predict the total pressure drop for bubble confinement flows. In the present study, their first correlation was compared with the data, and it under predicted the data with a MAE of 88.87%.

The comparison summarized above and in Fig. 26 showed that the flow boiling pressure drop data was predicted very well by the correlations of Mishima and Hibiki [73] and Keepaiboon et al. [77] with a mean absolute error of 18.7% and 19.2%, respectively.

5. Conclusions

Flow boiling characteristics of HFE-7100 in a horizontal rectangular multi-microchannels heat sink with a hydraulic diameter of 0.46 mm was experimentally investigated. The flow pattern features were visualized using a high-speed camera mounted on a microscope. All experiments were conducted at system pressure of 1 bar, inlet sub-cooling near 5 K, base heat flux ranging from 21.7–335.3 kW/m² and mass flux of 50–250 kg/m²s. The following points can be concluded from the present study:

1. Four flow patterns were observed during the experiments; bubbly, slug, churn and annular flow. More nucleation sites were seen with increasing heat flux. At high heat fluxes, the observed

bubbles had larger size compared to those at low heat fluxes. The flow patterns changed from slug to bubbly flow, when the mass flux increased for a given heat flux.

2. In some experiments, few small nucleating bubbles in the liquid film of slug and annular flow were captured. Therefore, there is a possibility for the contribution of both liquid film evaporation and nucleation in the liquid film especially at high heat fluxes.
3. All examined maps could predict annular flow data with a reasonable accuracy, while there was no general agreement for the prediction of bubbly, slug and churn flows.
4. Flow reversal was observed for all mass fluxes due to the rapid bubble generation near the channel inlet and slug formation. This affected the flow patterns for given conditions. However, it did not significantly affect the flow boiling heat transfer results for the entire heat sink.
5. The local two-phase heat transfer coefficient was found to increase with increasing wall heat flux.
6. When the local vapour quality increased, the local two-phase heat transfer coefficient decreased. Moreover, a negligible effect of the mass flux was found at this scale and with this particular fluid.
7. The two-phase heat transfer results were fairly predicted well by the correlations of Mahmoud and Karayiannis [36], Liu and Winterton [56], Li and Jia [65] and Shah [68] with MAE values ranging from 13.84% to 21.04%.
8. The correlations by Mishima and Hibiki [73] and Keepaiboon et al. [77] were able to predict the two-phase pressure drop results with a MAE of 18.7% and 19.2%, respectively.
9. The present heat sink could achieve base heat flux up to 335.3 kW/m², for a hot chip area of 500 mm², at surface temperature less than 80 °C. Maximum two-phase heat transfer coefficient reached was 12.71 kW/m²K at a mass flux of 250 kg/m²s. Further studies were underway by varying the channel aspect ratio and mass flux in order to increase the upper limits of possible heat flux that can be dissipated by the heat sink.

Acknowledgement

Ali Al-Zaidi would like to thank the Iraqi Ministry of Higher Education and Scientific Research (MOHESR) for their financial support for his PhD programme at Brunel University London.

Nomenclature

A	Area, [m ²]
B	Vertical distance between thermocouple and channel bottom, [m]
Bd	Bond number, [-] $Bd = (\rho_l - \rho_g)gD_h^2\sigma^{-1}$
Bo	Boiling number, [-] $Bo = q''_w(Gi_{lg})^{-1}$
C	Chisholm parameter, dimensionless correction factor [-]
Co	Confinement number, [-] $Co = [\sigma/g\Delta\rho]^{0.5}/D_h$
C_p	Specific heat at constant pressure, [J/kgK]
D	Diameter, [m]
D_h	Hydraulic diameter, [m]
f	Fanning friction factor, [-]
Fr	Froude number, [-] $Fr = v_l^2G^2(gD_h)^{-1}$
g	Gravitational acceleration, [m/s ²]
G	Mass flux, [kg/m ² s]
H	Height, [m]
h, HTC	Heat transfer coefficient, [W/m ² K]
\bar{h}	Average heat transfer coefficient, [W/m ² K]
i	Specific enthalpy, [J/kg]
i_{lg}	Latent heat of vaporization, [J/kg]
J	superficial velocity, [m/s]
k	Thermal conductivity, [W/mK]
K_{90}	The loss coefficient of the 90 degree turns, [-]
K_∞	Dimensionless incremental pressure drop number, [-]
L	Length, [m]
L^*	Dimensionless length, [-]
m	Fin parameter, $\sqrt{2h/k_{cu}W_{fin}}$
\dot{m}	Mass flow rate, [kg/s]
M	Molecular mass, [kg/kmol]
MAE	Mean absolute error
N	Number of channels, number of data points, [-]
N_{co}	Convection number, [-] $N_{co} = (1 - x/x)^{0.8}(v_l/v_g)^{0.5}$
Nu	Nusselt number, [-] $Nu = hD_hk_l^{-1}$
\bar{Nu}	Average Nusselt number, [-] $\bar{Nu} = \bar{h}D_hk_l^{-1}$
$N\mu$	Viscosity number, [-]
P	Pressure, [Pa]
Per	Perimeter, [m]
Pr	Prandtl number, [-] $Pr = cp\mu k^{-1}$
P_R	Reduced pressure, [-] $P_R = P_i/P_{cr}$

q''	Heat flux, [W/m ²]
R_p	Maximum profile peak height, [μm]
Re	Reynolds number, [-] $Re = GD_h\mu_l^{-1}$
Re_{ls}	Superficial liquid Reynolds number, [-] $Re_{ls} = G(1-x)D_h\mu_l^{-1}$
Re_{gs}	Superficial vapour Reynolds number, [-] $Re_{gs} = GxD_h\mu_g^{-1}$
Su_{go}	Vapour only Suratman number, [-] $Su_{go} = \rho_g\sigma D_h\mu_g^{-2}$
T	Temperature, [K]
v	Specific volume, [m ³ /kg]
W	Width, [m]
We	Weber number, [-] $We = G^2D_h(\rho\sigma)^{-1}$
We_{ls}	Weber number based on liquid superficial velocity, [-] $We_{ls} = J_l^2D_h\rho_l/\sigma$
We_{gs}	Weber number based on gas superficial velocity, [-] $We_{gs} = J_g^2D_h\rho_g/\sigma$
x	Vapour quality, [-]
X	Lockhart–Martinelli parameter, [-] $X = [(dP/dz)_l/(dP/dz)_g]^{0.5}$
Z	Axial distance, [m]

Greek Symbols

α	Area ratio, [-] $\alpha = H_{ch}W_{ch}N/H_{ch}W_b$
β	Aspect ratio, [-] $\beta = W_{ch}/H_{ch}$
ΔP	Pressure drop, [Pa]
ΔT	Temperature difference, [K]
ΔT_{LM}	Log mean temperature difference, [K]
η	Fin efficiency, [-]
θ	Percentage predicted within $\pm 30\%$ of data
μ	Viscosity, [Pa s]
ρ	Density, [kg/m ³]
σ	Surface tension, [N/m]
\emptyset	Two-phase pressure drop multiplier, [-]

Subscripts

3	Based on three-sided heat transfer in rectangular channel
4	Based on four-sided heat transfer in rectangular channel
acc	Acceleration
app	Apparent
b	Base
cb	Convective boiling
ch	Channel
cr	Critical
cu	Copper

<i>exp</i>	Experiment
<i>F</i>	Frictional
<i>f</i>	Fluid
<i>FD</i>	Fully developed
<i>fin</i>	Channel fin
<i>fr</i>	Friction
<i>g</i>	Gas or vapour
<i>h</i>	Heated
<i>HP</i>	Heated perimeter
<i>ht</i>	Heat transfer
<i>i</i>	Inlet
<i>ip</i>	Inlet plenum
<i>l</i>	Liquid
<i>ll</i>	Laminar liquid- laminar vapour
<i>lt</i>	Laminar liquid- turbulent vapour
<i>meas</i>	Measured
<i>nb</i>	Nucleate boiling
<i>o</i>	Exit
<i>op</i>	Outlet plenum
<i>pred</i>	Predicted
<i>sat</i>	Saturation
<i>sc</i>	Sudden contraction
<i>se</i>	Sudden expansion
<i>sp</i>	Single-phase
<i>sub</i>	Subcooled
<i>th</i>	Thermocouple
<i>tp</i>	Two-phase
<i>tl</i>	Turbulent liquid- laminar vapour
<i>tt</i>	Turbulent liquid-turbulent vapour
<i>w</i>	Wall, wetted
<i>wi</i>	Internal wall surface
<i>z</i>	Axial local

References

- [1] L. Cheng and G. Xia, "Fundamental issues, mechanisms and models of flow boiling heat transfer in microscale channels," *Int. J. Heat Mass Transf.*, vol. 108, pp. 97–127, 2017.
- [2] T. G. Karayiannis, M. M. Mahmoud, and D. B. R. Kenning, "A study of discrepancies in flow boiling results in small to microdiameter metallic tubes," *Exp. Therm. Fluid Sci.*, vol. 36, pp. 126–142, 2012.
- [3] T. G. Karayiannis and M. M. Mahmoud, "Flow boiling in microchannels: Fundamentals and applications," *Appl. Therm. Eng.*, vol. 115, pp. 1372–1397, 2017.
- [4] M. M. Mahmoud and T. G. Karayiannis, "Flow Boiling in Mini to Micro Diameter Channels," in *Encyclopaedia of Two-Phase Heat Transfer and Flow III*, John R. Thome, Ed. World Scientific Publishers, 2018.
- [5] T. G. Karayiannis and M. M. Mahmoud, "Flow Boiling in Micro-Passages : Developments in Fundamental Aspects and Applications," in *Proceedings of the 16th International Heat Transfer Conference, IHTC-16*, 2018.
- [6] J. Lee and I. Mudawar, "Fluid flow and heat transfer characteristics of low temperature two-phase micro-channel heat sinks - Part 1: Experimental methods and flow visualization results," *Int. J. Heat Mass Transf.*, vol. 51, no. 17–18, pp. 4315–4326, 2008.
- [7] J. Lee and I. Mudawar, "Fluid flow and heat transfer characteristics of low temperature two-phase micro-channel heat sinks - Part 2. Subcooled boiling pressure drop and heat transfer," *Int. J. Heat Mass Transf.*, vol. 51, no. 17–18, pp. 4327–4341, 2008.
- [8] J. Lee and I. Mudawar, "Critical heat flux for subcooled flow boiling in micro-channel heat sinks," *Int. J. Heat Mass Transf.*, vol. 52, no. 13–14, pp. 3341–3352, 2009.
- [9] K.-S. Yang, Y.-R. Jeng, C.-M. Huang, and C.-C. Wang, "Heat Transfer and Flow Pattern Characteristics for HFE-7100 Within Microchannel Heat Sinks," *Heat Transf. Eng.*, vol. 32, no. 7–8, pp. 697–704, 2011.
- [10] F. Yang, W. Li, X. Dai, and C. Li, "Flow boiling heat transfer of HFE-7000 in nanowire-coated microchannels," *Appl. Therm. Eng.*, vol. 93, pp. 260–268, 2016.
- [11] B. R. Fu, S. Y. Chung, W. J. Lin, L. Wang, and C. Pan, "Critical heat flux enhancement of HFE-7100 flow boiling in a minichannel heat sink with saw-tooth structures," *Adv. Mech. Eng.*, vol. 9, no. 2, pp. 1–10, 2017.
- [12] B.-R. Fu, C.-Y. Lee, and C. Pan, "The effect of aspect ratio on flow boiling heat transfer of HFE-7100 in a microchannel heat sink," *Int. J. Heat Mass Transf.*, vol. 58, no. 1–2, pp. 53–61, 2013.
- [13] C. C. Wang, W. J. Chang, C. H. Dai, Y. T. Lin, and K. S. Yang, "Effect of inclination on the convective boiling performance of a microchannel heat sink using HFE-7100," *Exp. Therm. Fluid Sci.*, vol. 36, pp. 143–148, 2012.
- [14] L. C. Hsu, S. W. Cion, K. W. Lin, and C. C. Wang, "An experimental study of inclination on the boiling heat transfer characteristics of a micro-channel heat sink using HFE-7100," *Int. Commun. Heat Mass Transf.*, vol. 62, pp. 13–17, 2015.
- [15] A. H. Al-Zaidi, M. M. Mahmoud, and T. G. Karayiannis, "Condensation Flow Patterns and Heat Transfer in Horizontal Microchannels," *Exp. Therm. Fluid Sci.*, vol. 90, pp. 153–173, 2018.
- [16] R. Remsburg, *Thermal design of electronic equipment*. 2001.
- [17] R. J. Phillips, "Forced Convection, Liquid Cooled, Microchannel Heat Sinks," Cambridge, 1988.
- [18] R. K. Shah and A. L. London, *Laminar flow forced convection in ducts, Supplement 1 to*

Advances in Heat Transfer. Academic Press New York, 1978.

- [19] T. Chen and S. V. Garimella, "Effects of Dissolved Air on Subcooled Flow Boiling of a Dielectric Coolant in a Microchannel Heat Sink," *J. Electron. Packag.*, vol. 128, no. 4, pp. 398–404, 2006.
- [20] H. W. Coleman and W. G. Steele, *Experimentation and uncertainty analysis for engineers*, 3rd ed. New York: Wiley, Chichester, 2009.
- [21] K. Stephan and P. Preuber, "Warmeubergang und Maximale Warmestromdichte Beim Behaltersieden Binarer und Ternarer Flussigkeitsgemische," *Chem. Ing. Tech.*, vol. 51, p. 37, 1979.
- [22] P. X. Jiang, M. H. Fan, G. S. Si, and Z. P. Ren, "Thermal Hydraulic Performance of Small Scale Micro-Channel and Porous-Media Heat Exchangers," *Int. J. Heat Mass Transf.*, vol. 44, pp. 1039–1051, 2001.
- [23] M. Mirmanto, "Single-phase flow and flow boiling of water in horizontal rectangular microchannels," Brunel University London (PhD thesis), London, UK, 2013.
- [24] D. Liu, P. S. Lee, and S. V. Garimella, "Prediction of the onset of nucleate boiling in microchannel flow," *Int. J. Heat Mass Transf.*, vol. 48, no. 25, pp. 5134–5149, 2005.
- [25] U. Soupremanien, S. Le Person, M. Favre-Marinet, and Y. Bultel, "Influence of the aspect ratio on boiling flows in rectangular mini-channels," *Exp. Therm. Fluid Sci.*, vol. 35, pp. 797–809, 2011.
- [26] E. M. Fayyadh, M. M. Mahmoud, K. Sefiane, and T. G. Karayiannis, "Flow boiling heat transfer of R134a in multi microchannels," *Int. J. Heat Mass Transf.*, vol. 110, pp. 422–436, 2017.
- [27] W. Qu and I. Mudawar, "Prediction and measurement of incipient boiling heat flux in micro-channel heat sinks," *Int. J. Heat Mass Transf.*, vol. 45, no. 19, pp. 3933–3945, 2002.
- [28] J. Li and P. Cheng, "Bubble cavitation in a microchannel," *Int. J. Heat Mass Transf.*, vol. 47, no. 12, pp. 2689–2698, 2004.
- [29] T. Harirchian and S. V. Garimella, "Effects of channel dimension, heat flux, and mass flux on flow boiling regimes in microchannels," *Int. J. Multiph. Flow*, vol. 35, no. 4, pp. 349–362, 2009.
- [30] N. Borhani and J. R. Thome, "Intermittent dewetting and dryout of annular flows," *Int. J. Multiph. Flow*, vol. 67, pp. 144–152, 2014.
- [31] M. K. Akbar, D. A. Plummer, and S. M. Ghiaasiaan, "On gas-liquid two-phase flow regimes in microchannels," *Int. J. Multiph. Flow*, vol. 29, pp. 855–865, 2003.
- [32] T. Harirchian and S. V. Garimella, "A comprehensive flow regime map for microchannel flow boiling with quantitative transition criteria," *Int. J. Heat Mass Transf.*, vol. 53, no. 13, pp. 2694–2702, 2010.
- [33] E. Costa-Patry and J. R. Thome, "Flow pattern-based flow boiling heat transfer model for microchannels," *Int. J. Refrig.*, vol. 36, no. 2, pp. 414–420, 2013.
- [34] C. L. Ong and J. R. Thome, "Macro-to-microchannel transition in two-phase flow: Part 1 - Two-phase flow patterns and film thickness measurements," *Exp. Therm. Fluid Sci.*, vol. 35, no. 1, pp. 37–47, 2011.
- [35] S. S. Bertsch, E. A. Groll, and S. V. Garimella, "Refrigerant flow boiling heat transfer in parallel microchannels as a function of local vapor quality," *Int. J. Heat Mass Transf.*, vol. 51, pp. 4775–4787, 2008.
- [36] M. M. Mahmoud and T. G. Karayiannis, "Heat transfer correlation for flow boiling in small to

- micro tubes,” *Int. J. Heat Mass Transf.*, vol. 66, pp. 553–574, 2013.
- [37] H. Huang and J. R. Thome, “An experimental study on flow boiling pressure drop in multi-microchannel evaporators with different refrigerants,” *Exp. Therm. Fluid Sci.*, vol. 80, pp. 391–407, 2017.
- [38] S. M. Zivi, “Estimation of steady-state steamvoid-fraction by means of the principle of minimum entropy production,” *J. Heat Transf.*, vol. 86, pp. 247–252, 1964.
- [39] W. Qu and I. Mudawar, “Flow boiling heat transfer in two-phase micro-channel heat sinks-I. Experimental investigation and assessment of correlation methods,” *Int. J. Heat Mass Transf.*, vol. 46, no. 15, pp. 2755–2771, 2003.
- [40] Y. Wang and K. Sefiane, “Effects of heat flux, vapour quality, channel hydraulic diameter on flow boiling heat transfer in variable aspect ratio micro-channels using transparent heating,” *Int. J. Heat Mass Transf.*, vol. 55, pp. 2235–2243, 2012.
- [41] M. Mirmanto, “Local pressure measurements and heat transfer coefficients of flow boiling in a rectangular microchannel,” *Heat Mass Transf.*, vol. 52, pp. 73–83, 2016.
- [42] G. M. Lazarek and S. H. Black, “Evaporative heat transfer, pressure drop and critical heat flux in a small vertical tube with R-113,” *Int. J. Heat Mass Transf.*, vol. 25, no. 7, pp. 945–960, 1982.
- [43] Z. Y. Bao, D. F. Fletcher, and B. S. Haynes, “Flow boiling heat transfer of Freon R11 and HCFC123 in narrow passages,” *Int. J. Heat Mass Transf.*, vol. 43, pp. 3347–3358, 2000.
- [44] E. Sobierska, R. Kulenovic, R. Mertz, and M. Groll, “Experimental results of flow boiling of water in a vertical microchannel,” *Exp. Therm. Fluid Sci.*, vol. 31, pp. 111–119, 2006.
- [45] J. Pettersen, “Flow vaporization of CO₂ in microchannel tubes,” *Exp. Therm. Fluid Sci.*, vol. 28, no. 2–3, pp. 111–121, 2004.
- [46] H.-K. Oh and C.-H. Son, “Flow boiling heat transfer and pressure drop characteristics of CO₂ in horizontal tube of 4.57-mm inner diameter,” *Appl. Therm. Eng.*, vol. 31, pp. 163–172, 2011.
- [47] T.-W. Lim, S.-S. You, J.-H. Choi, and H.-S. Kim, “Experimental Investigation of Heat Transfer in Two-phase Flow Boiling,” *Exp. Heat Transf.*, vol. 28, pp. 23–36, 2015.
- [48] A. M. Al-Gaheeshi, M. M. Mahmoud, and T. G. Karayiannis, “Flow boiling heat transfer in a vertical small-diameter tube: Effect of different fluids and surface characteristics,” in *Proceedings of the 4th International Forum on Heat Transfer*, 2016, pp. 1–9.
- [49] H. Tuo and P. Hrnjak, “Periodical reverse flow and boiling fluctuations in a microchannel evaporator of an air-conditioning system,” *Int. J. Refrig.*, vol. 36, pp. 1263–1275, 2013.
- [50] T. Chen and S. V. Garimella, “Measurements and high-speed visualizations of flow boiling of a dielectric fluid in a silicon microchannel heat sink,” *Int. J. Multiph. Flow*, vol. 32, no. 8, pp. 957–971, 2006.
- [51] L. Consolini and J. R. Thome, “Micro-channel flow boiling heat transfer of R-134a, R-236fa, and R-245fa,” *Microfluid. Nanofluidics*, vol. 6, no. 6, pp. 731–746, 2009.
- [52] S. M. Kim and I. Mudawar, “Review of databases and predictive methods for heat transfer in condensing and boiling mini/micro-channel flows,” *Int. J. Heat Mass Transf.*, vol. 77, pp. 627–652, 2014.
- [53] S. Wang, X. Bi, and S. Wang, “Boiling heat transfer in small rectangular channels at low Reynolds number and mass flux,” *Exp. Therm. Fluid Sci.*, vol. 77, pp. 234–245, 2016.
- [54] M. M. Shah, “Chart correlation for saturated boiling heat transfer: equations and further study,” *ASHRAE Trans.*, vol. 88, no. 1, pp. 185–196, 1982.

- [55] S. G. Kandlikar, "A General Correlation for Saturated Two-Phase Flow Boiling Heat Transfer Inside Horizontal and Vertical Tubes," *J. Heat Transfer*, vol. 112, p. 219, 1990.
- [56] Z. Liu and R. H. S. Winterton, "A general correlation for saturated and subcooled flow boiling in tubes and annuli, based on a nucleate pool boiling equation," *Int. J. Heat Mass Transf.*, vol. 34, pp. 2759–2766, 1991.
- [57] M. G. Cooper, "Heat Flow Rates in Saturated Nucleate Pool Boiling-A Wide-Ranging Examination Using Reduced Properties," *Adv. Heat Transf.*, vol. 16, pp. 157–239, 1984.
- [58] G. R. Warrier, V. K. Dhir, and L. A. Momoda, "Heat transfer and pressure drop in narrow rectangular channels," *Exp. Therm. Fluid Sci.*, vol. 26, no. 1, pp. 53–64, 2002.
- [59] J. Lee and I. Mudawar, "Two-phase flow in high-heat-flux micro-channel heat sink for refrigeration cooling applications: Part II - Heat transfer characteristics," *Int. J. Heat Mass Transf.*, vol. 48, no. 5, pp. 941–955, 2005.
- [60] L. Sun and K. Mishima, "An evaluation of prediction methods for saturated flow boiling heat transfer in mini-channels," *Int. J. Heat Mass Transf.*, vol. 52, pp. 5323–5329, 2009.
- [61] W. Li and Z. Wu, "A general correlation for evaporative heat transfer in micro/mini-channels," *Int. J. Heat Mass Transf.*, vol. 53, no. 9, pp. 1778–1787, 2010.
- [62] S.-M. Kim and I. Mudawar, "Universal approach to predicting saturated flow boiling heat transfer in mini/micro-channels – Part II. Two-phase heat transfer coefficient," *Int. J. Heat Mass Transf.*, vol. 64, pp. 1239–1256, 2013.
- [63] J. C. Chen, "A correlation for boiling heat transfer to saturated fluids in convective flow," *Ind. Eng. Chem.*, vol. 5, pp. 322–329, 1966.
- [64] D. F. Sempértegui-Tapia and G. Ribatski, "Flow boiling heat transfer of R134a and low GWP refrigerants in a horizontal micro-scale channel," *Int. J. Heat Mass Transf.*, vol. 108, pp. 2417–2432, 2017.
- [65] X. Li and L. Jia, "The investigation on flow boiling heat transfer of R134a in micro-channels," *J. Therm. Sci.*, vol. 24, no. 5, pp. 452–462, 2015.
- [66] P. Thiangtham *et al.*, "An experimental study on two-phase flow patterns and heat transfer characteristics during boiling of R134a flowing through a multi-microchannel heat sink," *Int. J. Heat Mass Transf.*, vol. 98, pp. 390–400, 2016.
- [67] B. Markal, O. Aydin, and M. Avci, "Prediction of Heat Transfer Coefficient in Saturated Flow Boiling Heat Transfer in Parallel Rectangular Microchannel Heat Sinks: An Experimental Study," *Heat Transf. Eng.*, vol. 38, no. 16, pp. 1415–1428, 2017.
- [68] M. M. Shah, "Unified correlation for heat transfer during boiling in plain mini/micro and conventional channels," *Int. J. Refrig.*, vol. 74, pp. 606–626, 2017.
- [69] E. A. Pike-Wilson and T. G. Karayiannis, "Flow boiling of R245fa in 1.1mm diameter stainless steel, brass and copper tubes," *Exp. Therm. Fluid Sci.*, vol. 59, pp. 166–183, 2014.
- [70] D. Sempértegui-tapia and G. Ribatski, "The effect of the cross-sectional geometry on saturated flow boiling heat transfer in horizontal micro-scale channels," in *IV Journeys in Multiphase Flows (JEM 2015)*, 2015.
- [71] M. M. Mahmoud and T. G. Karayiannis, "Performance of a Micro Scale Integrated Thermal Management System," in *5th Micro and Nano Flows Conference*, 2016, no. 11–14 September, pp. 1–2.
- [72] R. W. Lockhart and R. C. Martinelli, "Proposed Correlation of Data for Isothermal Two-Phase, Two-Component Flow in Pipes," *Chemical Engineering Progress*, vol. 45, no. 1, pp. 39–48,

1949.

- [73] K. Mishima and T. Hibiki, "Some characteristics of air-water two-phase flow in small diameter vertical tubes," *Int. J. Multiph. Flow*, vol. 22, no. 4, pp. 703–712, 1996.
- [74] W. Qu and I. Mudawar, "Measurement and prediction of pressure drop in two-phase micro-channel heat sinks," *Int. J. Heat Mass Transf.*, vol. 46, no. 15, pp. 2737–2753, 2003.
- [75] P. Lee and S. V. Garimella, "Saturated flow boiling heat transfer and pressure drop in silicon microchannel arrays," *Int. J. Heat Mass Transf.*, vol. 51, no. 3, pp. 789–806, 2008.
- [76] S. M. Kim and I. Mudawar, "Universal approach to predicting two-phase frictional pressure drop for mini/micro-channel saturated flow boiling," *Int. J. Heat Mass Transf.*, vol. 58, no. 1–2, pp. 718–734, 2013.
- [77] C. Keepaiboon, P. Thiangtham, O. Mahian, A. S. Dalkılıç, and S. Wongwises, "Pressure drop characteristics of R134a during flow boiling in a single rectangular micro-channel," *Int. Commun. Heat Mass Transf.*, vol. 71, pp. 245–253, 2016.
- [78] X. Li and T. Hibiki, "Frictional pressure drop correlation for two-phase flows in mini and micro multi-channels," *Appl. Therm. Eng.*, vol. 116, pp. 316–328, 2017.
- [79] B. Markal, O. Aydin, and M. Avci, "Prediction of Pressure Drop for Flow Boiling in Rectangular Multi-Microchannel Heat Sinks," *Heat Transf. Eng.*, vol. 0, no. 0, pp. 1–13, 2017.
- [80] J. G. Collier and J. R. Thome, *Convective Boiling and Condensation*, Third edit. Oxford, UK: Oxford University Press, 1994.
- [81] M. M. Mahmoud, T. G. Karayiannis, and D. B. R. Kenning, "Flow boiling pressure drop of R134a in microdiameter tubes: Experimental results and assessment of correlations," *Heat Transf. Eng.*, vol. 35, no. 2, pp. 178–192, 2014.

Appendix I: Single-phase correlations.

Author(s)	Correlation	Remarks
Shah and London [18]	$f_{app} = \frac{3.44}{Re\sqrt{L^*}} + \frac{f_{FD}Re + \frac{K_{\infty}}{4L^*} - 3.44/\sqrt{L^*}}{Re(1 + C(L^*)^{-2})}$ $L^* = L/Re * D_h$	For laminar developing flow in non-circular ducts
	$f_{FD} = (24(1 - 1.355\beta + 1.946\beta^2 - 1.7012\beta^3 + 0.9564\beta^4 - 0.2537\beta^5))/Re$	For laminar fully developed flow in non-circular ducts
Stephan and Preuber [21]	$Nu = 4.364 + \frac{0.086(RePrD_h/L)^{1.33}}{1 + 0.1Pr(ReD_h/L)^{0.83}}$	For laminar developing flow in a single passage
Jiang et al. [22]	<p>For $L^* < 0.05$</p> $Nu = 0.52 * (L^*)^{-0.62}$ <p>For $L^* > 0.05$</p> $Nu = 2.02 * (L^*)^{-0.31}$ $L^* = L/RePrD_h$	For laminar flow in rectangular multi-microchannels
Mirmanto [23]	$Nu = Re^{0.283}Pr^{-0.513}(L^*)^{-0.309}$	For laminar developing flow in a single rectangular microchannel

Appendix IIa: Flow boiling heat transfer correlations. The definitions used in Appendix IIa are given in Appendix IIb.

Author(s)	Correlation	Remarks
Recommended for macrochannels		
Shah [54]	$h_{tp} = \text{Max}(E, S)h_{sp}$ $S = 1.8/N^{0.8}$ <p>For $1 < N$:</p> $E = 230Bo^{0.5} \quad (\text{for } Bo > 3 \times 10^{-5})$ $E = 1 + 46Bo^{0.5} \quad (\text{for } Bo < 3 \times 10^{-5})$ <p>For $0.1 < N \leq 1$:</p> $E = FBo^{0.5} \exp(2.74N^{-0.1})$ <p>For $N \leq 1$:</p> $E = FBo^{0.5} \exp(2.47N^{-0.15})$ $F = 14.7 \quad (\text{for } Bo \geq 11 \times 10^{-4})$ $F = 15.43 \quad (\text{for } Bo < 11 \times 10^{-4})$ $N = N_{co} \quad (\text{for } Fr \geq 0.04)$ $N = 0.38Fr^{-0.3}N_{co} \quad (\text{for } Fr < 0.04)$	<p>D = 6–25.4 mm</p> <p>Fluids (water, R11, R12, R22, R113, cyclohexane)</p> <p>For saturated boiling in vertical and horizontal channels</p>
Kandlikar [55]	$h_{tp} = \text{Max}(E, S)h_{sp}$ $E = 0.6683N_{co}^{-0.2}f(Fr) + 1058Bo^{0.7}F_{fl}$ $S = 1.136N_{co}^{-0.9}f(Fr) + 667.2Bo^{0.7}F_{fl}$ $f(Fr) = 1 \quad (\text{for } Fr \geq 0.04)$ $f(Fr) = (25Fr)^{0.3} \quad (\text{for } Fr < 0.04)$ <p>Where F_{fl} is:</p> <p>Water: 1 R11: 1.3 R12: 1.5 R22: 2.2 R113: 1.3 R134a: 1.63 R152a: 1.1</p>	<p>D = 4–32 mm</p> <p>Fluids (water, R11, R12, R22, R113, R134a, R152a)</p> <p>G = 13–8179 kg/m²s q" = 0.3–228 kW/m²</p> <p>For saturated boiling in vertical and horizontal tubes</p>
Liu and Winterton [56]	$h_{tp} = \sqrt{(Eh_{sp})^2 + (Sh_{coop})^2}$ $E = \left(1 + xPr \left(\frac{v_g}{v_l} - 1\right)\right)^{0.35}$ $h_{coop} = 55P_R^{0.12-0.2\log_{10}Rp} (-\log_{10}(P_R))^{-0.55} M^{-0.5} q_w''^{0.67}$ $S = (1 + 0.055E^{0.1}Re^{0.16})^{-1}$	<p>D = 2.95–32 mm</p> <p>Fluids (water, R11, R12, R113, R114, R22, ethylene glycol)</p> <p>G = 12.4–8179.3 kg/m²s q" = 0.35–2620 kW/m²</p> <p>For vertical and horizontal channels</p>
Recommended for mini/microchannels		
Lazarek and Black [42]	$h_{tp} = 30Re^{0.857}Bo^{0.714} \frac{k_l}{D_h}$	<p>D = 3.1 mm</p> <p>Fluid (R113)</p> <p>q" = 14–380 kW/m² G = 125–750 kg/m²s</p> <p>For nucleate boiling dominant in a single vertical tube</p>

Warrier et al. [58]	$h_{tp} = [1 + 6Bo^{\frac{1}{16}} - 5.3(1 - 855Bo)x^{0.65}]h_{sp}$	$D_h = 0.75 \text{ mm}$ Fluid (FC-84) $G = 557\text{--}1600 \text{ kg/m}^2\text{s}$ $q'' = \text{up to } 59.9 \text{ kW/m}^2$ For saturated boiling in horizontal rectangular multi-channels
Lee and Mudawar [59]	$h_{tp} = 3.856X^{0.267}h_{sp} \quad (\text{for } 0 < x < 0.05)$ $h_{tp} = 436.48Bo^{0.522}We^{0.351}X^{0.665}h_{sp} \quad (\text{for } 0.05 < x < 0.55)$ $h_{tp} = \text{Max}\{(108.6X^{1.665}h_{sp,g}), h_{sp,g}\} \quad (\text{for } 0.55 < x < 1)$ $h_{sp,g} = \frac{Nu_3k_g}{D_h} \quad (\text{for laminar vapour flow})$ $h_{sp,g} = 0.023Re_{gs}^{0.8}Pr_g^{0.4} \frac{k_g}{D_h} \quad (\text{for turbulent vapour flow})$	$D_h = 0.348 \text{ mm}$ Fluids (water, R134a) $G = 127\text{--}654 \text{ kg/m}^2\text{s}$ $q'' = 159\text{--}938 \text{ kW/m}^2$ For saturated boiling in horizontal rectangular multi-channels
Sun and Mishima [60]	$h_{tp} = \frac{6Re^{1.05}Bo^{0.54}k_l}{We^{0.191}(\rho_l/\rho_g)^{0.142}D_h}$	$D_h = 0.21\text{--}6.05 \text{ mm}$ Fluids (water, R11, R12, R123, R134a, R141b, R22, R404A, R407C, R410A, CO ₂) $G = 44\text{--}1500 \text{ kg/m}^2\text{s}$ $q'' = 5\text{--}109 \text{ kW/m}^2$ For saturated boiling in vertical and horizontal (single and multi) channels
Li and Wu [61]	$h_{tp} = 334Bo^{0.3}(BdRe_{ls}^{0.36})^{0.4} \frac{k_l}{D_h}$	$D = 0.16\text{--}3.1 \text{ mm}$ Fluids (water, R11, R12, R123, R134a, R22, R410A, R236fa, R245fa, CO ₂ , FC-72, ethanol, propane) For saturated boiling in vertical and horizontal (single and multi) channels
Kim and Mudawar [62]	$h_{tp} = \sqrt{(h_{nb})^2 + (h_{cb})^2}$ $h_{nb} = \left[2345 \left(Bo \frac{P_{er,h}}{P_{er,w}} \right)^{0.7} Pr^{0.38} (1-x)^{-0.51} \right] \left[0.023Re_{ls}^{0.8} Pr^{0.4} \frac{k_l}{D_h} \right]$ $h_{cb} = \left[5.2 \left(Bo \frac{P_{er,h}}{P_{er,w}} \right)^{0.08} We^{-0.54} + 3.5 \left(\frac{1}{X_{tt}} \right)^{0.94} \left(\frac{\rho_g}{\rho_l} \right)^{0.25} \right] \left[0.023Re_{ls}^{0.8} Pr^{0.4} \frac{k_l}{D_h} \right]$ $P_{er,h} = 2H_{ch} + W_{ch}$ $P_{er,w} = 2H_{ch} + 2W_{ch}$	$D_h = 0.19\text{--}6.5 \text{ mm}$ Fluids (water, FC-72, R11, R113, R123, R1234yf, R1234ze, R134a, R152a, R22, R236fa, R245fa, R32, R404A, R407C, R410A, R417A, CO ₂) $G = 19\text{--}1608 \text{ kg/m}^2\text{s}$ $q'' = 5\text{--}109 \text{ kW/m}^2$ For saturated boiling in vertical and horizontal (single and multi) channels
Mahmoud and Karayiannis [36]	$h_{tp} = Sh_{coop} + Fh_{sp}$ $S = \frac{1}{1 + 2.56 \times 10^{-6} (Re_{ls} F^{1.25})^{1.17}}$ $F = \left(1 + \frac{A}{X} \right)^{0.64}$ $A = 2.812C_o^{-0.408}$	$D = 0.52\text{--}4.26 \text{ mm}$ Fluid (R134a) $G = 100\text{--}700 \text{ kg/m}^2\text{s}$ $q'' = 1.7\text{--}158 \text{ kW/m}^2$ For saturated boiling in vertical single tubes

Li and Jia [65]	<p>For nucleate boiling regime:</p> $h_{tp} = 189Bo^{0.178}Bd^{0.4}Re_{ls}^{0.12}\frac{k_l}{D_h}$ <p>For convective boiling regime:</p> $h_{tp} = 277.3Bo^{0.978}Re_{ls}^{0.94}(1-x)^{0.47}\frac{k_l}{D_h}$ <p>(Not clear at the onset which equation is used in comparisons)</p>	<p>$D_h = 0.5$ mm Fluid (R134a) $G = 373.33-1244.44$ kg/m²s $q'' = \text{up to } 802.12$ kW/m² For saturated boiling in horizontal rectangular multi-channels</p>
Lim et al. [47]	$h_{tp} = \frac{Re^{0.196}k_l}{Bo^{0.117}C_{FR}^{0.42}D_h}$ $C_{FR} = 0.4905 + Fr(1 - x^{3.134})$	<p>$D_h = 0.5$ mm Fluid (water) $G = 200-600$ kg/m²s $q'' = 100-400$ kW/m² For saturated boiling in horizontal square single channel</p>
Thiangtham et al. [66]	$h_{tp} = \frac{10^{16.7}Bo^{0.3}We^{2.7}k_l}{Re^{4.95}(\rho_l/\rho_g)^{0.9}D_h}$	<p>$D_h = 0.421$ mm Fluid (R134a) $G = 150-600$ kg/m²s $q'' = 3-127$ kW/m² $T_{sat} = 13, 18, 23$ °C For saturated boiling in horizontal rectangular multi-channels</p>
Markal et al. [67]	$h_{tp} = \frac{0.054Re_{ls}^{0.214}Bo^{0.913}\beta^{0.552}\left(\frac{1-x}{x}\right)^{0.7}\left(\frac{k_l}{D_h}\right)^{1.959}}{We^{0.094}Pr^{0.333}}$	<p>Different aspect ratios: 0.37–5 at constant $D_h =$ 0.1 mm Different hydraulic diameters: 0.1–0.25 mm at constant aspect ratio: 1 Fluid (de-ionized water) $G = 51-728.7$ kg/m²s $q'' = 36-221.7$ kW/m² $x = 0.01-0.69$ $7.72 \leq Re_{ls} \leq 190$ For saturated boiling in horizontal rectangular multi-channels</p>
Shah [68]	$h_{tp} = Fh_{Shah(1982)}$ $F = 2.1 - 0.008We_g - 110Bo$ <p>If $F < 1$, use $F = 1$.</p> <p>If the channel is fully heated, use $D_h = D_{HP}$ If the channel is partially heated, use D_h in We_g and Fr. Also, use D_{HP} in other expressions.</p> $D_{HP} = \frac{4Flow\ Area}{Perimeter\ with\ heat\ transfer}$	<p>$D = 0.38-27.1$ mm Fluids (Water, CO₂, R11, R12, R22, R32, R113, R123, R114, R123, R134a, R152a, R1234yf, R236fa, R245fa, ammonia, propane, isobutane, carbon tetrachloride, isopropyl alcohol, ethanol, methanol, n-butanol, cyclohexane, benzene, heptane, pentane, argon, hydrogen, nitrogen, helium) $G = 15-2437$ kg/m²s For saturated boiling in vertical and horizontal (single and multi) channels</p>

Appendix IIb: Details on the definitions that are used in Appendix IIa.

$$Re_{ls} = G(1-x)D_h/\mu_l$$

$$Re_{gs} = GxD_h/\mu_g$$

$$h_{sp} = \frac{Nu_3 k_l}{D_h} \quad (\text{for } Re_{ls} < 2000)$$

$$h_{sp} = 0.023 Re_{ls}^{0.8} Pr^{0.4} \frac{k_l}{D_h} \quad (\text{for } Re_{ls} > 3000)$$

$$Nu_3 = 8.235(1 - 1.833\beta + 3.767\beta^2 - 5.814\beta^3 + 5.361\beta^4 - 2\beta^5) \quad (\text{for three walls heat transfer, Shah and London [18]})$$

For $Re_{ls} < 2000$ and $Re_{gs} < 2000$:

$$X_{ll} = \left(\frac{\mu_l}{\mu_g}\right)^{0.5} \left(\frac{1-x}{x}\right)^{0.5} \left(\frac{\rho_g}{\rho_l}\right)^{0.5}$$

For $Re_{ls} < 2000$ and $Re_{gs} \geq 2000$:

$$X_{lt} = \left(\frac{f_l}{f_g}\right)^{0.5} \left(\frac{1-x}{x}\right)^{1.0} \left(\frac{\rho_g}{\rho_l}\right)^{0.5}$$

For $Re_{ls} \geq 2000$ and $Re_{gs} < 2000$:

$$X_{tl} = \left(\frac{f_l}{f_g}\right)^{0.5} \left(\frac{1-x}{x}\right)^{1.0} \left(\frac{\rho_g}{\rho_l}\right)^{0.5}$$

For $Re_{ls} \geq 2000$ and $Re_{gs} \geq 2000$:

$$X_{tt} = \left(\frac{\mu_l}{\mu_g}\right)^{0.1} \left(\frac{1-x}{x}\right)^{0.9} \left(\frac{\rho_g}{\rho_l}\right)^{0.5}$$

Fanning friction factor:

$$f_k = \frac{24}{Re_{ks}} (1 - 1.355\beta + 1.946\beta^2 - 1.7012\beta^3 + 0.9564\beta^4 - 0.2537\beta^5) \quad (\text{for } Re_{ks} < 2000 \text{ "rectangular channel, Shah and London [18]"})$$

$$f_k = \frac{0.079}{Re_{ks}^{0.25}} \quad (\text{for } 2000 \leq Re_{ks} < 20,000)$$

$$f_k = \frac{0.046}{Re_{ks}^{0.2}} \quad (\text{for } Re_{ks} \geq 20,000)$$

(k) refers to l or g

Appendix III: Correlations and model for two-phase frictional pressure drop.

Author(s)	Correlation	Remarks
Recommended for conventional channels		
Lockhart and Martinelli [72]	$\left(\frac{dP}{dz}\right)_F = \left(\frac{dP}{dz}\right)_f \phi_l^2$ $\phi_l^2 = 1 + \frac{C}{X} + \frac{1}{X^2}$ $X^2 = \frac{(dP/dz)_l}{(dP/dz)_g}$ <p>C=5 (for laminar liquid-laminar vapour) C=12 (for laminar liquid-turbulent vapour) C=10 (for turbulent liquid- laminar vapour) C=20 (for turbulent liquid-turbulent vapour)</p>	D = 1.5–25.8 mm Fluids (air/water, air/benzene, air/kerosene and air/oils) Circular horizontal channels
Homogenous flow model, Collier and Thome [80]	$\Delta P_{acc} = G^2 v_{lg} x_o$ $\Delta P_{fr} = \frac{2f_{tp} G^2 v_l L_{tp}}{D_h} \left[1 + \frac{x_o}{2} \left(\frac{v_{lg}}{v_l}\right)\right]$ $v_{lg} = v_g - v_l$ <p>$f_{tp} = 0.003$ as recommended by Qu and Mudawar [74]</p>	
Recommended for mini/microchannels		
Mishima and Hibiki [73]	$\left(\frac{dP}{dz}\right)_F = \left(\frac{dP}{dz}\right)_f \phi_l^2$ $\phi_l^2 = 1 + \frac{C}{X} + \frac{1}{X^2}$ $X^2 = \frac{(dP/dz)_l}{(dP/dz)_g}$ $C = 21(1 - e^{-0.319 \cdot 10^3 D_h})$	D = 1.05–4.08 mm Fluids (Air-water, ammonia, R113-N ₂) Circular and rectangular channels Horizontal and vertical flow
Qu and Mudawar [74]	$\left(\frac{dP}{dz}\right)_F = \left(\frac{dP}{dz}\right)_f \phi_l^2$ $\phi_l^2 = 1 + \frac{C}{X} + \frac{1}{X^2}$ $X^2 = \frac{(dP/dz)_l}{(dP/dz)_g}$ $C = 21(1 - e^{-319 D_h})(0.00418G + 0.0613)$	$D_h = 0.35$ mm Fluid (Water) Horizontal, rectangular multi-channels
Lee and Garimella [75]	$\left(\frac{dP}{dz}\right)_F = \left(\frac{dP}{dz}\right)_f \phi_l^2$ $\phi_l^2 = 1 + \frac{C}{X} + \frac{1}{X^2}$ $X^2 = \frac{(dP/dz)_l}{(dP/dz)_g}$ $C = 2566G^{0.5466} D_h^{0.8819} (1 - e^{-319 D_h})$	$D_h = 0.162$ – 0.571 mm Fluid (Water) Horizontal rectangular multi-channels

Kim and Mudawar [76]	$\left(\frac{dP}{dz}\right)_F = \left(\frac{dP}{dz}\right)_f \phi_l^2$ $\phi_l^2 = 1 + \frac{C}{X} + \frac{1}{X^2}$ $X^2 = \frac{(dP/dz)_l}{(dP/dz)_g}$ <p>For $Re_{ls} < 2000$:</p> $C = C^*(1 + 530We^{0.52}(Bo \frac{P_{er,h}}{P_{er,w}})^{1.09})$ <p>For $Re_{ls} \geq 2000$:</p> $C = C^*(1 + 60We^{0.32}(Bo \frac{P_{er,h}}{P_{er,w}})^{0.78})$ <p>For $Re_{ls} < 2000$ and $Re_{gs} < 2000$:</p> $C^* = 3.5 * 10^{-5} Re^{0.44} Su_{go}^{0.5} \left(\frac{\rho_l}{\rho_g}\right)^{0.48}$ <p>For $Re_{ls} < 2000$ and $Re_{gs} \geq 2000$:</p> $C^* = 0.0015 Re^{0.59} Su_{go}^{0.19} \left(\frac{\rho_l}{\rho_g}\right)^{0.36}$ <p>For $Re_{ls} \geq 2000$ and $Re_{gs} < 2000$:</p> $C^* = 8.7 * 10^{-4} Re^{0.17} Su_{go}^{0.5} \left(\frac{\rho_l}{\rho_g}\right)^{0.14}$ <p>For $Re_{ls} \geq 2000$ and $Re_{gs} \geq 2000$:</p> $C^* = 0.39 Re^{0.03} Su_{go}^{0.1} \left(\frac{\rho_l}{\rho_g}\right)^{0.35}$ $P_{er,h} = 2H_{ch} + W_{ch}$ $P_{er,w} = 2H_{ch} + 2W_{ch}$	$D_h = 0.349-5.35$ mm Fluids (R12, R22, R134a, R245fa, R410a, FC-72, CO ₂ , ammonia and water) Circular and rectangular channels Horizontal and vertical flow
Keepaiboon et al. [77]	$\left(\frac{dP}{dz}\right)_F = \left(\frac{dP}{dz}\right)_f \phi_l^2$ $\phi_l^2 = 1 + \frac{C}{X} + \frac{1}{X^2}$ $X^2 = \frac{(dP/dz)_l}{(dP/dz)_g}$ $C = 1.93 * 10^5 Re^{-1.18} Co^{-27.99} X^{0.93}$	$D_h = 0.68$ mm Fluid (R134a) Horizontal single rectangular channel
Huang and Thome [37]	$\left(\frac{dP}{dz}\right)_F = \left(\frac{dP}{dz}\right)_f \phi_l^2$ $\phi_l^2 = 1 + \frac{C}{X} + \frac{1}{X^2}$ $X^2 = \frac{(dP/dz)_l}{(dP/dz)_g}$ <p>For $Re_{ls} \leq 2000$ and R1233zd(E):</p> $f_l = \frac{8.058}{Re_{ls}}$ <p>For $Re_{ls} \leq 2000$ and others: f_l: is obtained from Shah and London [18]</p> <p>For $Re_{ls} > 2000$:</p> $f_l = \frac{0.079}{Re_{ls}^{-0.25}}$ <p>For $Re_{ls} \leq 2000$ and $Re_{gs} \leq 2000$:</p> $C = 0.0037 Re_{gs}^{1.7} Re^{-0.83}$ <p>For $Re_{ls} \leq 2000$ and $Re_{gs} > 2000$:</p> $C = 0.9 Re_{gs}^{0.034} Re^{0.2}$	$D_h = 0.1$ mm Fluid (R1233zd(E), R245fa and R236fa) Horizontal square multi-channels

$$\left(\frac{dP}{dz}\right)_F = \left(\frac{dP}{dz}\right)_f \phi_l^2$$

$$\phi_l^2 = 1 + \frac{C}{X} + \frac{1}{X^2}$$

$$X^2 = \frac{(dP/dz)_l}{(dP/dz)_g}$$

For turbulent liquid-turbulent vapour:

$$C = 7.63 Re_{tp}^{0.66} x^{0.43} N \mu_{tp}^{1.2}$$

For laminar liquid-turbulent vapour:

$$C = 2.23 Re_{tp}^{0.54} x^{0.25} N \mu_{tp}^{0.51}$$

For laminar liquid-laminar vapour:

$$C = 1.87 Re_{tp}^{0.38} x^{0.35} N \mu_{tp}^{0.12}$$

$$Re_{tp} = GD_h / \mu_{tp}$$

$$\frac{1}{\mu_{tp}} = \frac{1-x}{\mu_l} + \frac{x}{\mu_g}$$

$$N \mu_{tp} = \frac{1}{\left(\rho_{tp} \sigma \sqrt{\sigma / g \Delta \rho}\right)^{0.5}}$$

$$\rho_{tp} = x \rho_g + (1-x) \rho_l$$

$D = 0.109\text{--}2.13$
mm

Fluid (R134a,
R22, R404a,
R236fa, R245fa,
FC-72, CO₂,
water)
Multi-channels

Li and Hibiki
[78]

$$\left(\frac{dP}{dz}\right)_F = \left(\frac{dP}{dz}\right)_f \phi_l^2$$

$$\phi_l^2 = 1 + \frac{C}{X} + \frac{1}{X^2}$$

$$X^2 = \frac{(dP/dz)_l}{(dP/dz)_g}$$

$D_h = 0.1\text{--}0.25$ mm
Fluid (Deionized
water)
Horizontal
rectangular multi-
channels

Markal et al.
[79]

$$C = -7.1 + \left(\frac{(1-x_o)^{1.766}}{Re^{0.12} \beta^{0.031} Bo^{0.165} We^{0.074} \left(\frac{v_l}{v_g}\right)^{0.233} \left(\frac{L_{tp}}{D_h}\right)^{0.247}} \right)$$

List of tables

Table 1. Thermophysical properties of HFE-7100 at atmospheric pressure.

i_{lg} [J/kg]	ρ_l [kg/m ³]	ρ_g [kg/m ³]	k_f [W/mK]	C_p [J/kgK]	σ [N/m]
111661	1373	9.575	0.06206	1157	0.0136

Table 2. Geometric dimensions of the evaporator.

H_{ch} [mm]	W_{ch} [mm]	W_{fin} [mm]	N [-]	D_h [mm]	β [-]	$W_b \times L_b$ [mm]
0.35	0.7	0.1	25	0.466	2	20×25

Table 3. Experimental uncertainty.

Parameter	Uncertainty
Temperature T-type	±0.024K
Temperature K-type	±0.038–0.12K
Inlet pressure transducer	±0.46kPa
Outlet pressure transducer	±0.37kPa
Differential pressure	±0.08%
Coriolis mass flow rate	±0.1%
Fanning friction factor	±1.7–2.05%
Average Nusselt number	±3.69–6.47%
Local vapour quality	±0.68–10.2%
Local heat transfer coefficient	±1.6–13.48%
Mass flux	±0.32–0.64%
Heat flux	±0.44–6.88%

Table 4. Experimental operating conditions.

System pressure [bar]	1
Saturation temperature [°C]	59.6
Inlet sub-cooling [K]	5
Mass flux [kg/m ² s]	50–250
Base heat flux [kW/m ²]	21.7–335.3
Exit vapour quality [-]	Up to 0.99

List of figures

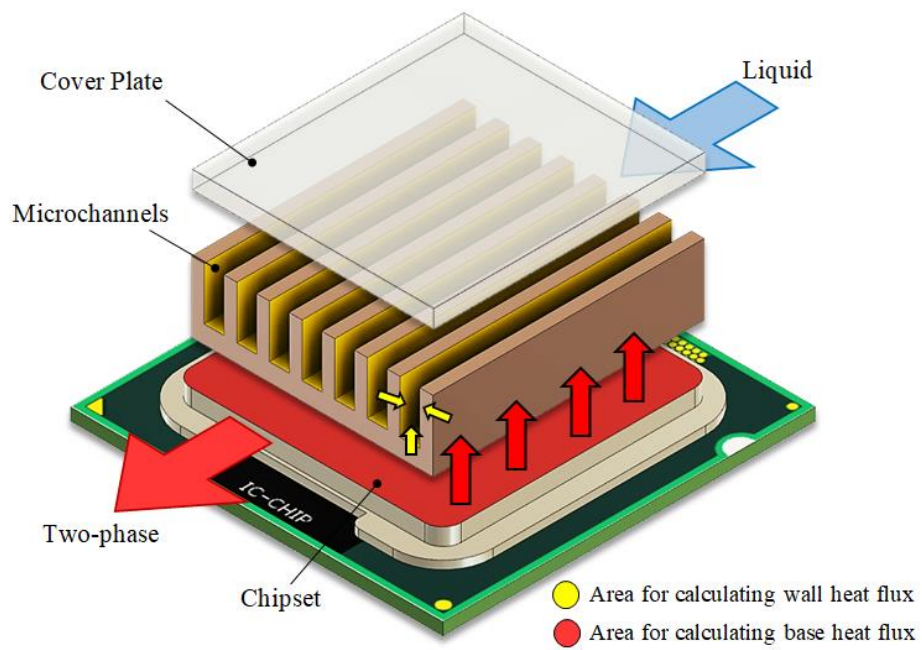


Fig. 1. Exploded drawing of flow boiling in multi-microchannels heat sink for cooling electronic components.

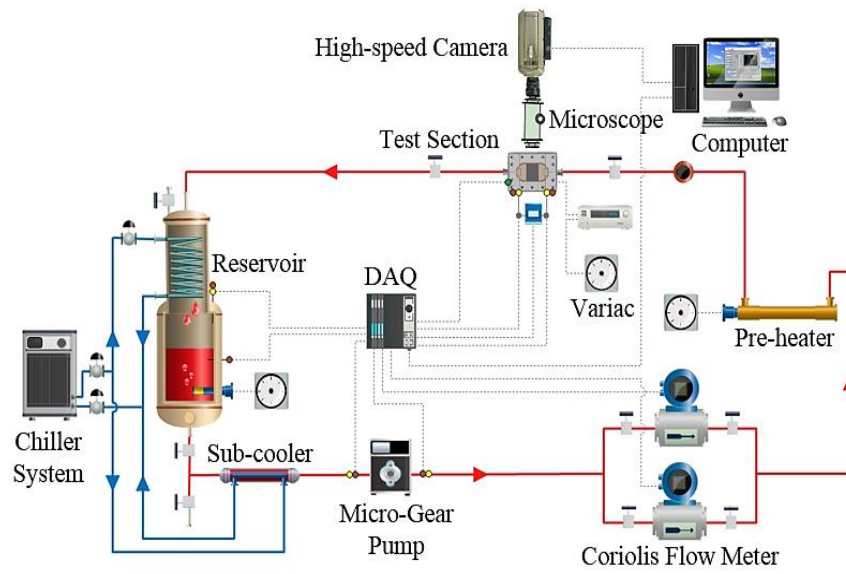


Fig. 2. Schematic diagram of the experimental facility.

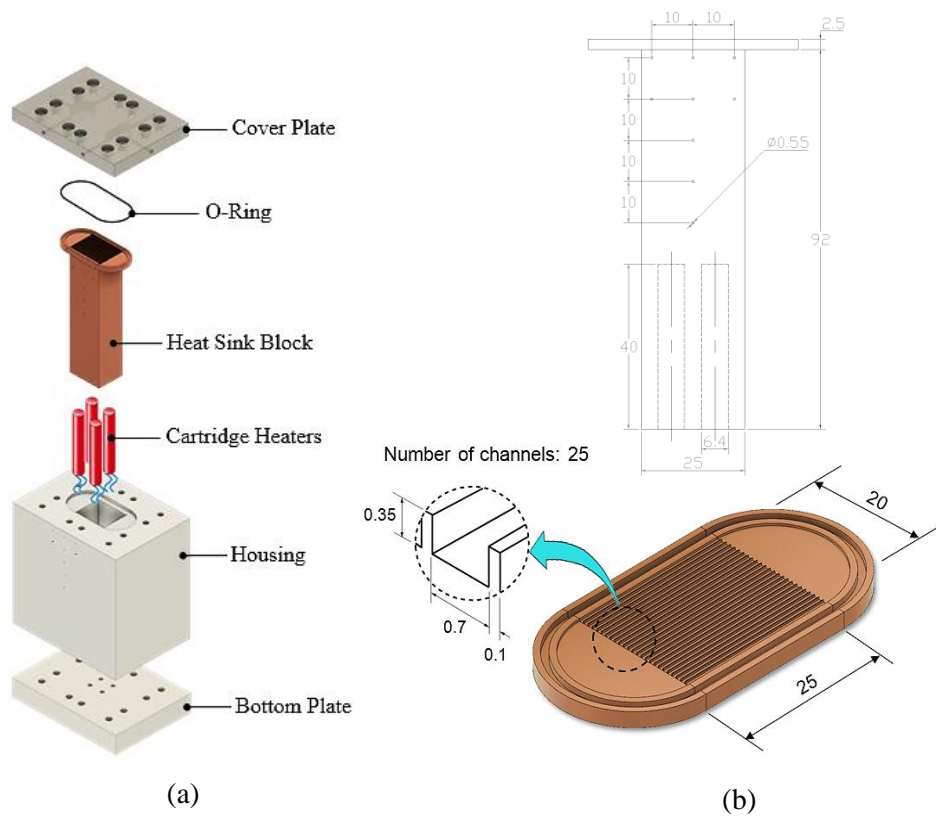
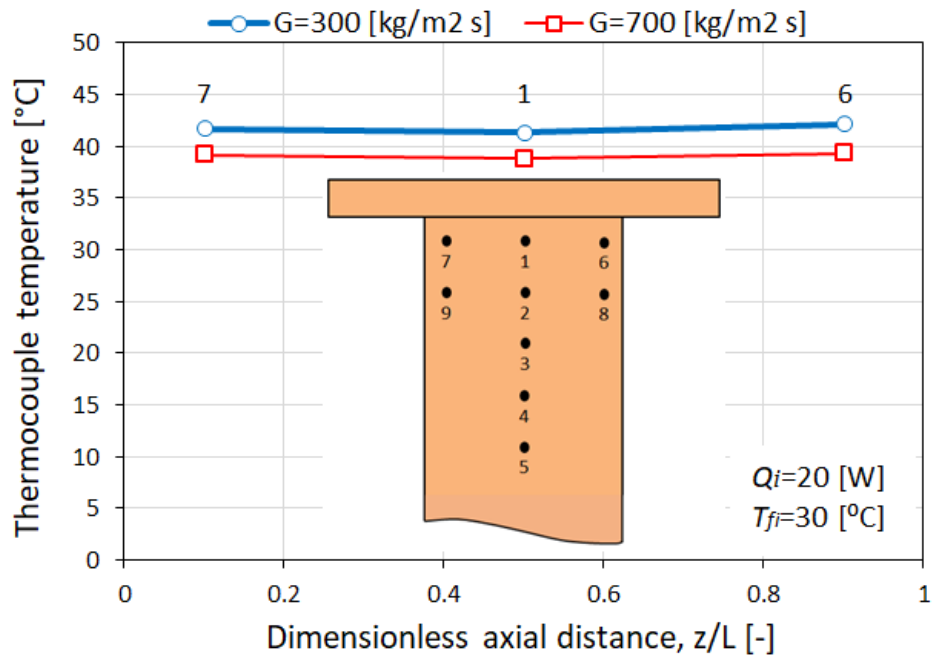
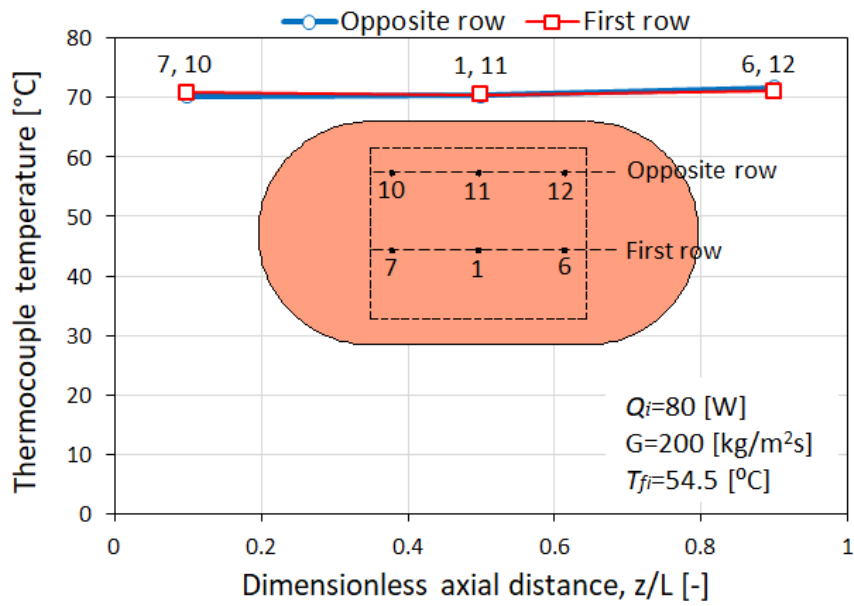


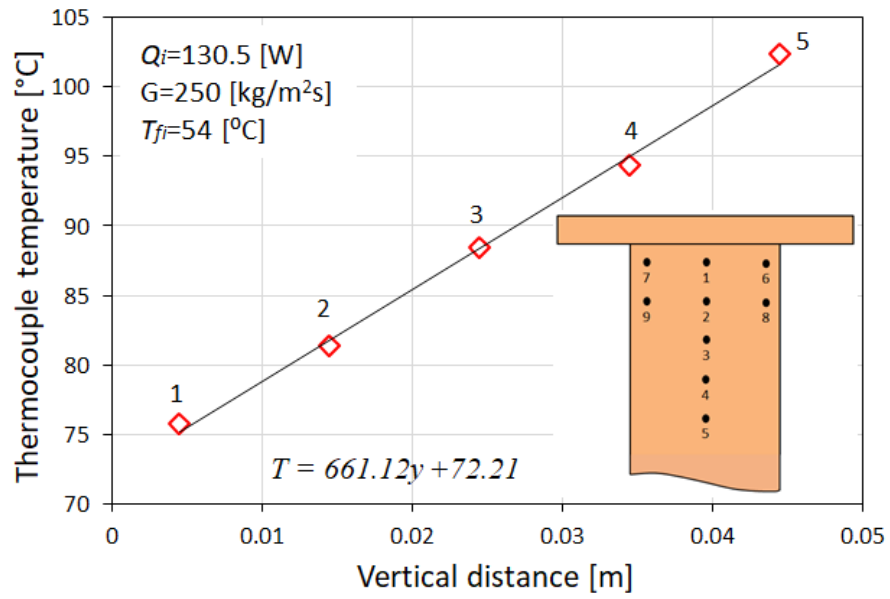
Fig. 3. Test section (a) exploded drawing, (b) heat sink. Dimensions in mm.



(a)

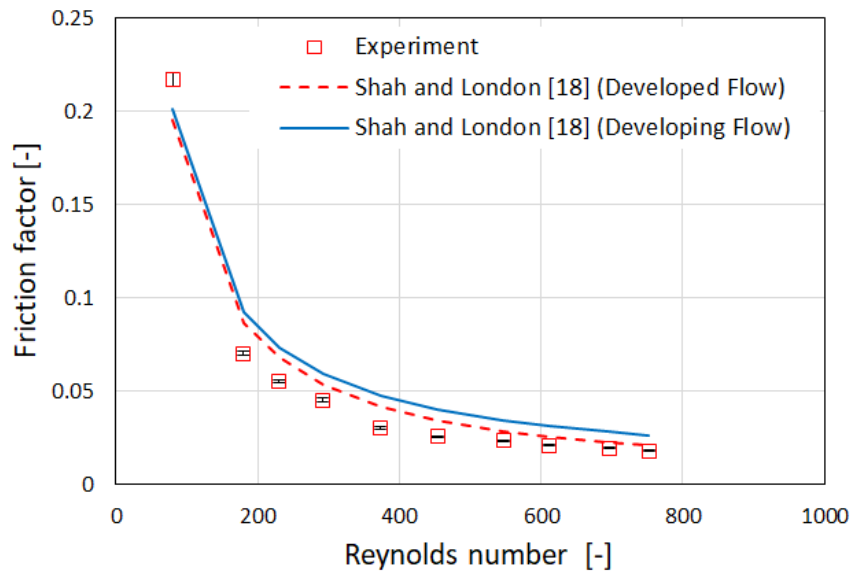


(b)

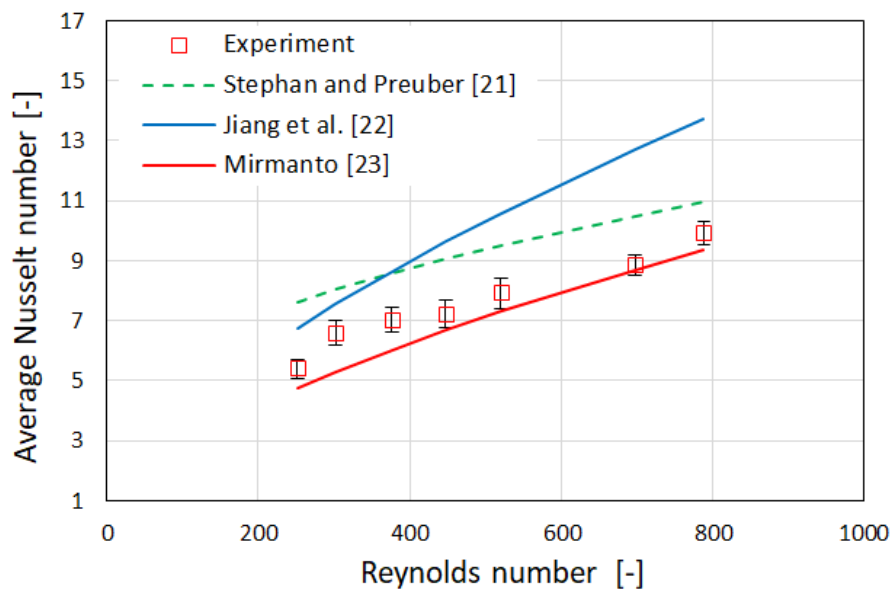


(c)

Fig. 4. Temperature distribution (a) in the axial direction during single-phase flow, (b) in the axial direction during two-phase flow for $G = 200$ kg/m²s and (c) in the vertical direction during two-phase flow for $G = 250$ kg/m²s.

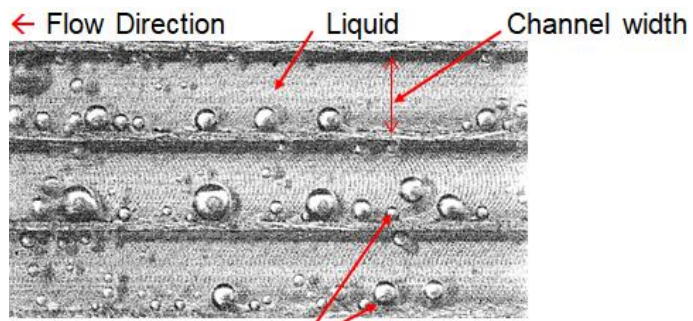


(a)



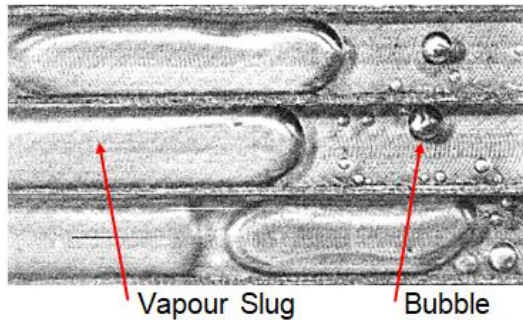
(b)

Fig. 5. Experimental single-phase (a) Fanning friction factor versus Reynolds number and (b) Nusselt number versus Reynold number.

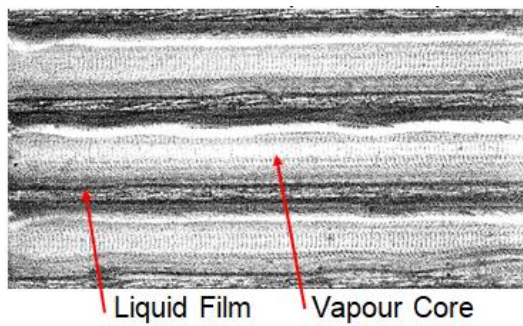


(a) Bubbly flow
(near channel inlet)

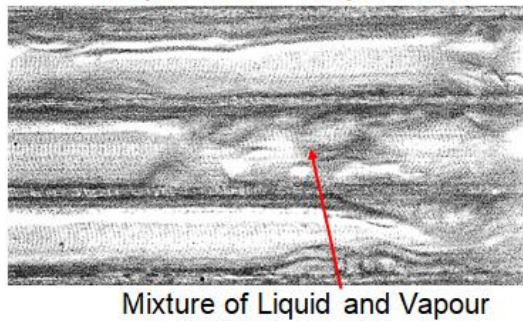
Bubbles start at channel corners



(b) Slug flow
(near channel middle)



(c) Annular flow
(near channel outlet)



(d) Churn flow
(near channel middle)

Fig. 6. Experimental flow patterns for mass flux of $50 \text{ kg/m}^2\text{s}$ at wall heat flux of 29.2 kW/m^2 (a, b and c) and at wall heat flux of 36 kW/m^2 (d).

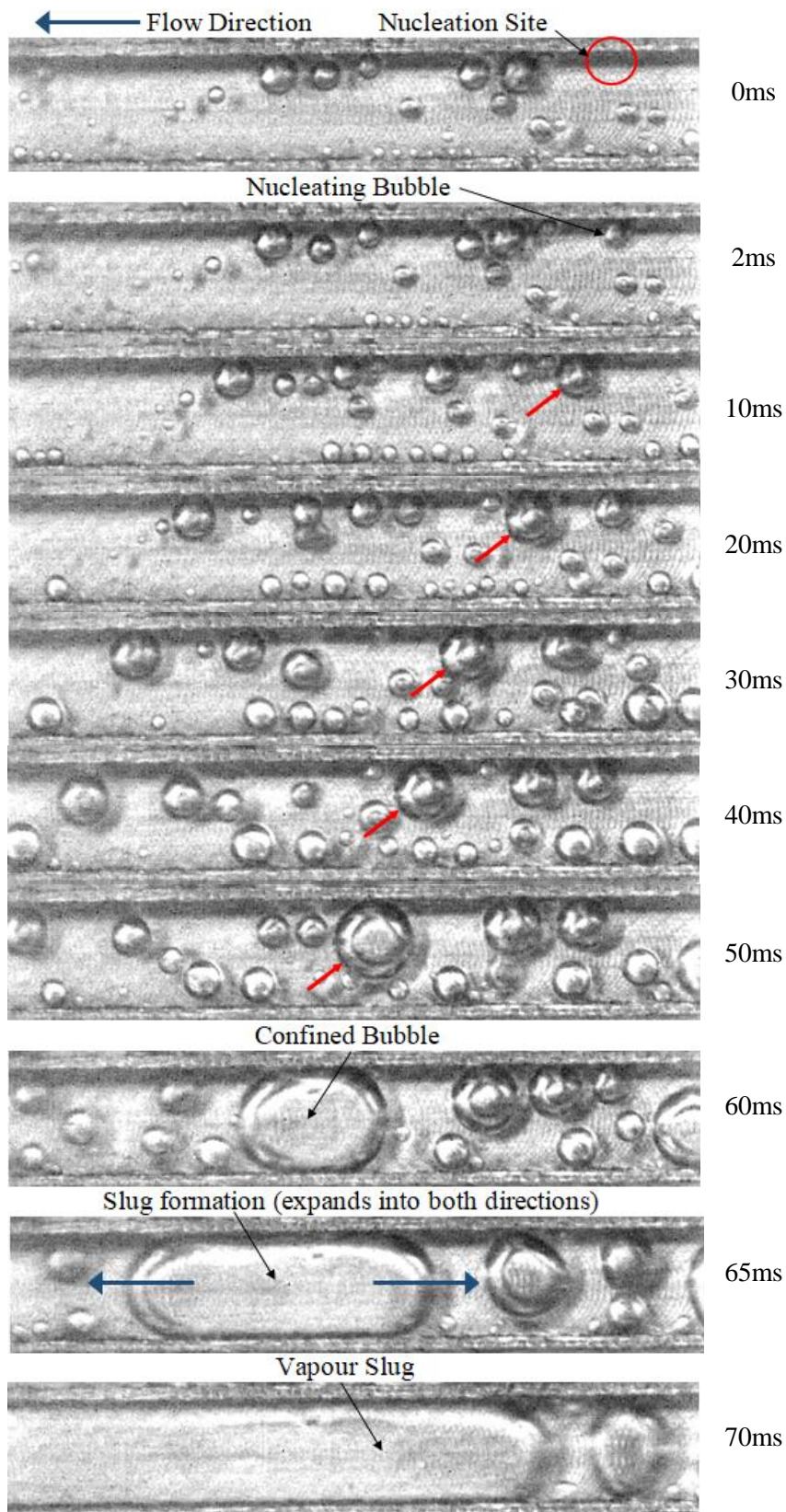


Fig. 7. Sequence of pictures of bubble growth near the channel inlet at wall heat flux of 29.2 kW/m^2 and mass flux of $50 \text{ kg/m}^2\text{s}$.

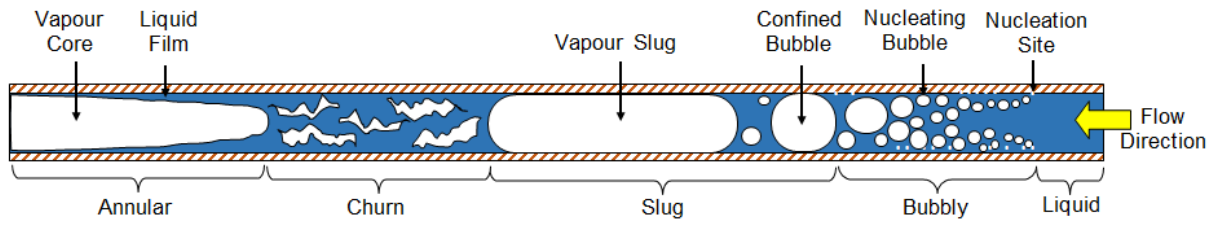


Fig. 8. Flow boiling structures observed in this study.

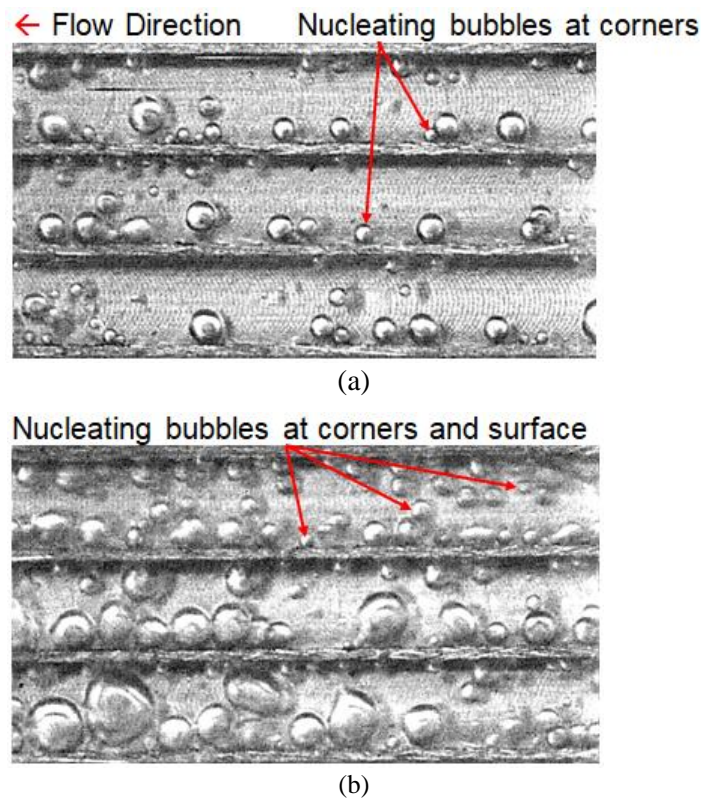


Fig. 9. Effect of heat flux on the bubbly flow (nucleation sites) at mass flux of $50 \text{ kg/m}^2\text{s}$, near the channel inlet and different wall heat fluxes (a) 29.2 kW/m^2 (b) 58.1 kW/m^2 .

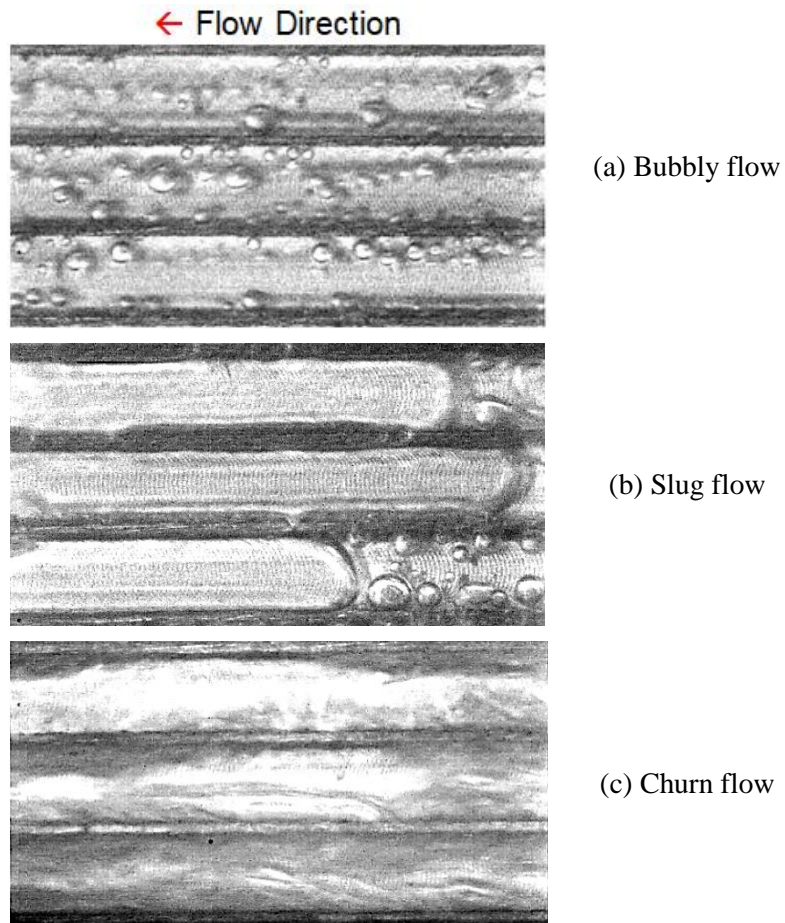


Fig. 10. Effect of heat flux on the flow patterns at mass flux of $150 \text{ kg/m}^2\text{s}$, near channel middle and three wall heat fluxes (a) 30.4 kW/m^2 (b) 58.3 kW/m^2 (c) 113.1 kW/m^2 .

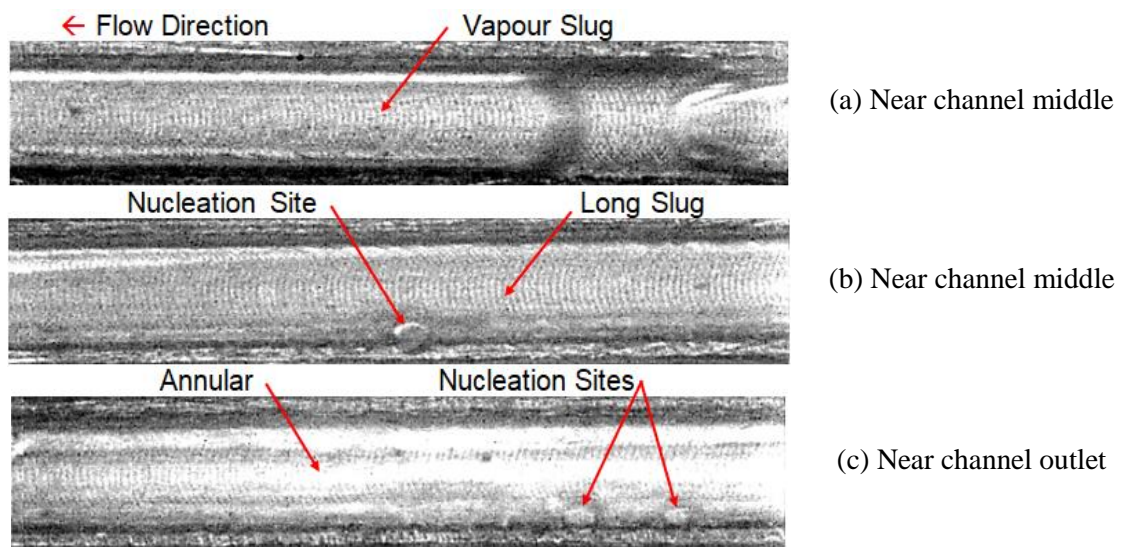


Fig. 11. Flow patterns at mass flux of $100 \text{ kg/m}^2\text{s}$ and three wall heat fluxes (a) 23.7 kW/m^2 (b) 46.5 kW/m^2 (c) 57.8 kW/m^2 .

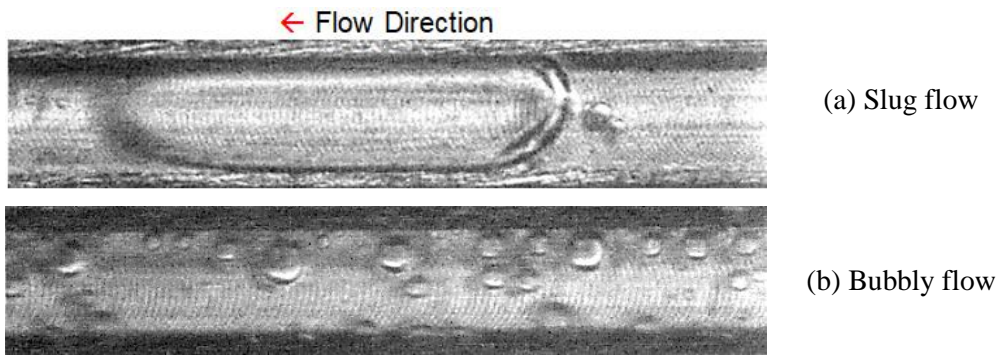


Fig. 12. Effect of mass flux on the flow patterns at wall heat flux of 25 kW/m^2 , near the channel middle and different mass fluxes (a) $50 \text{ kg/m}^2\text{s}$ (b) $250 \text{ kg/m}^2\text{s}$.

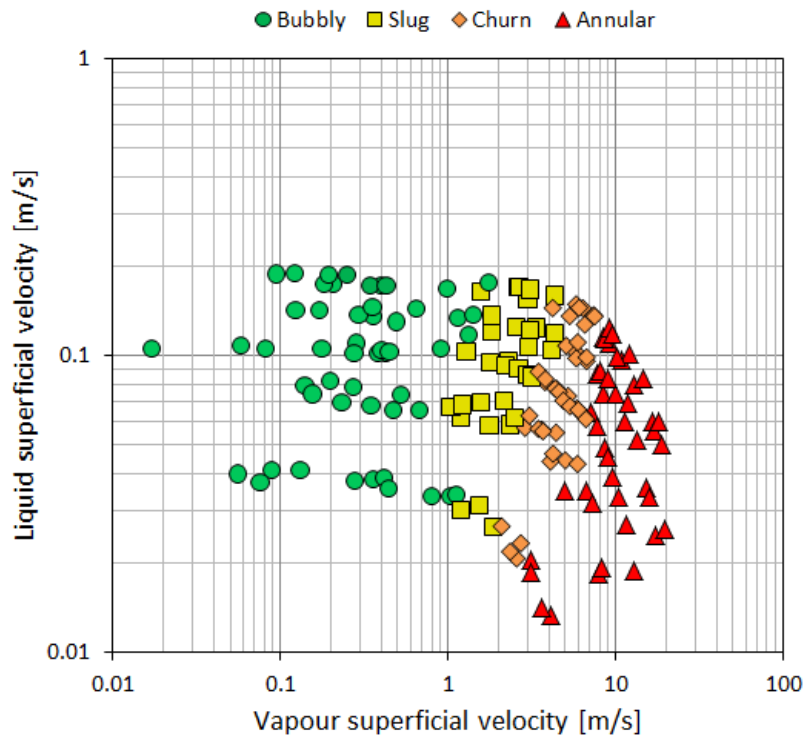


Fig. 13. Flow patterns map of HFE-7100 at wall heat flux ranging from 12.4 to 191.6 kW/m² and mass flux of 50–250 kg/m²s.

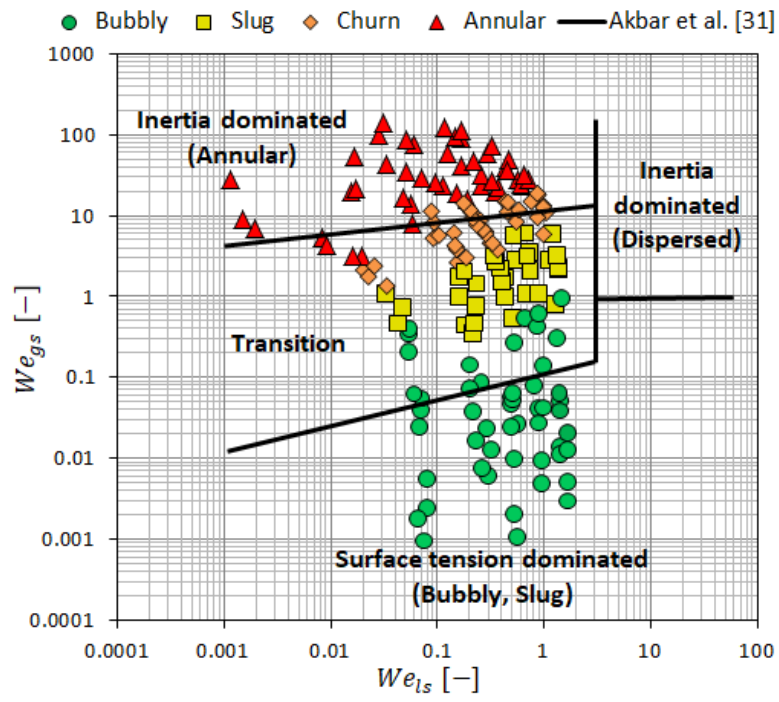


Fig. 14. Comparison of experimental data with the Akbar et al. [31] flow map.

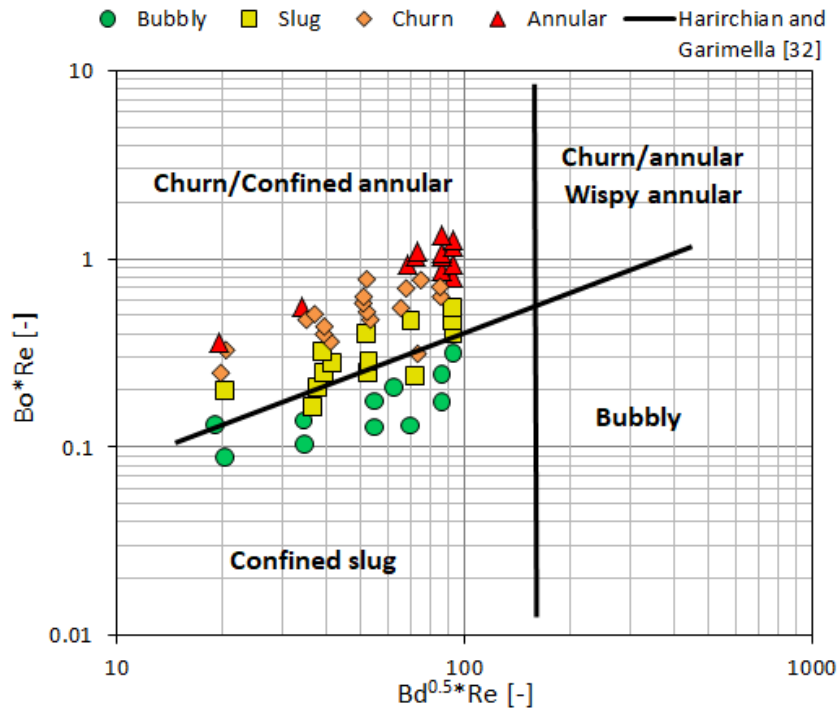


Fig. 15. Comparison of experimental data with the Harirchian and Garimella [32] flow map.

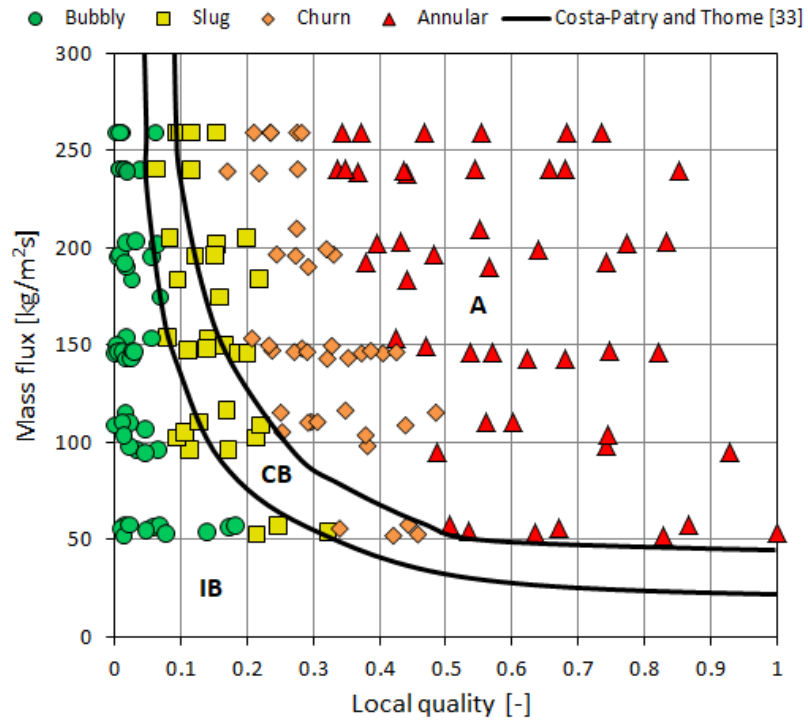


Fig. 16. Comparison of experimental data with the Costa-Patry and Thome [33] flow map.

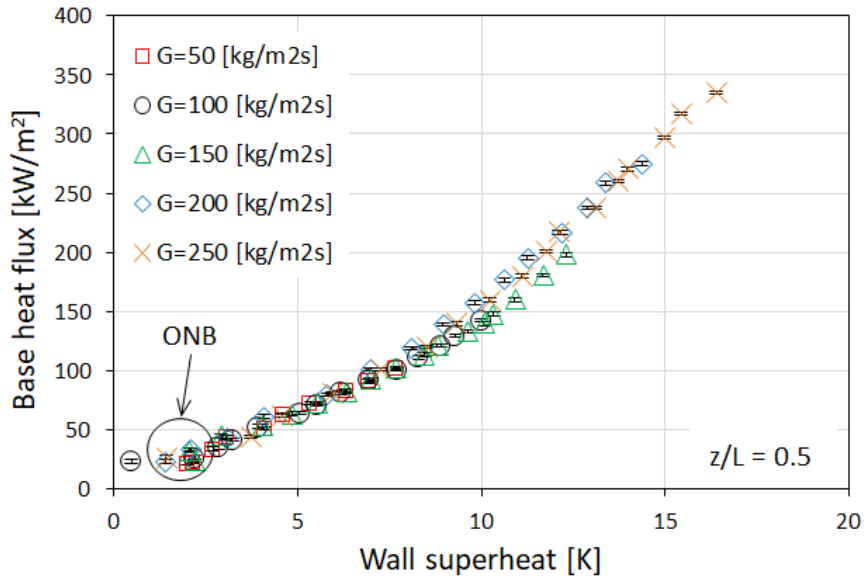


Fig. 17. Boiling curve of HFE-7100 at five mass fluxes and $z/L = 0.5$.

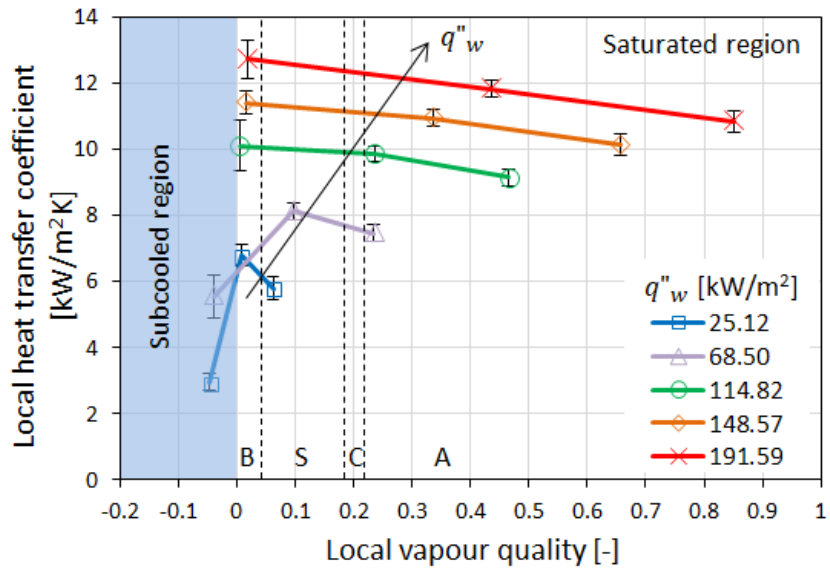


Fig. 18. Effect of wall heat flux at mass flux of $250 \text{ kg/m}^2\text{s}$; (B) bubbly (S) slug (C) churn (A) annular.

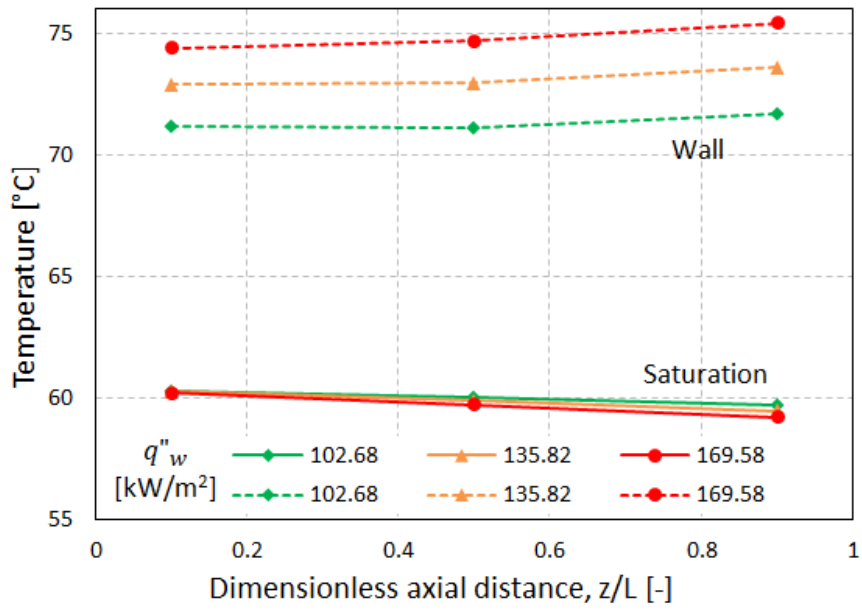


Fig. 19. Local saturation temperature and wall temperature at different wall heat fluxes and mass flux of $250 \text{ kg/m}^2\text{s}$.

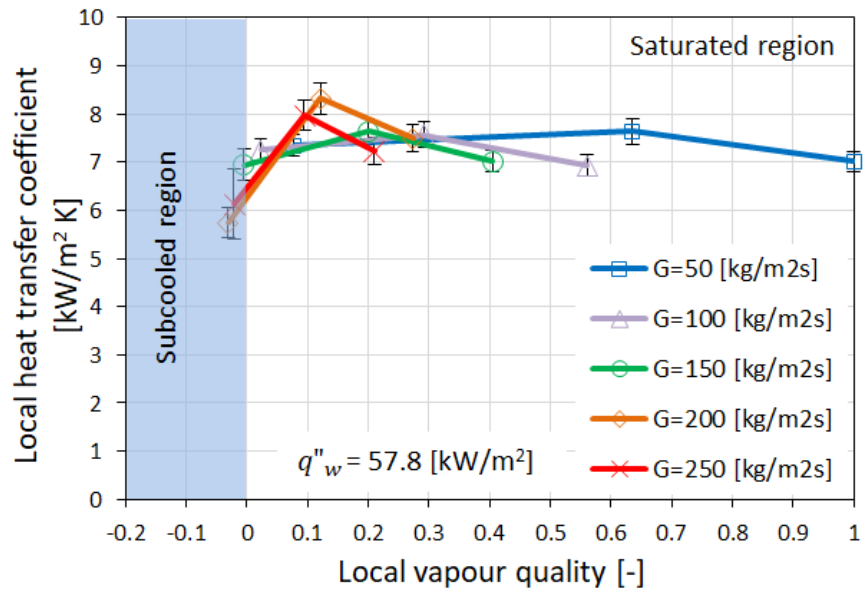


Fig. 20. Effect of mass flux on the local heat transfer coefficient at wall heat flux of 57.8 kW/m^2 .

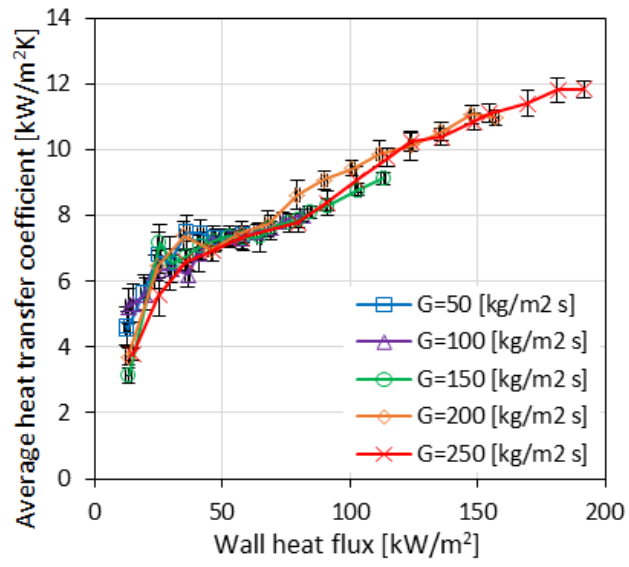


Fig. 21. Effect of wall heat flux and mass flux on the average heat transfer coefficient.

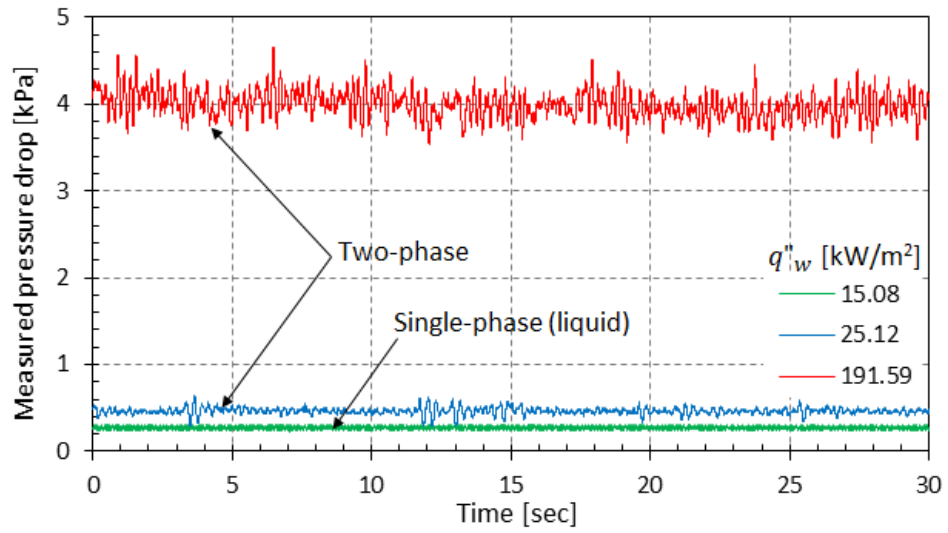


Fig. 22. Measured pressure drop fluctuation at different wall heat fluxes and mass flux of 250 kg/m²s.

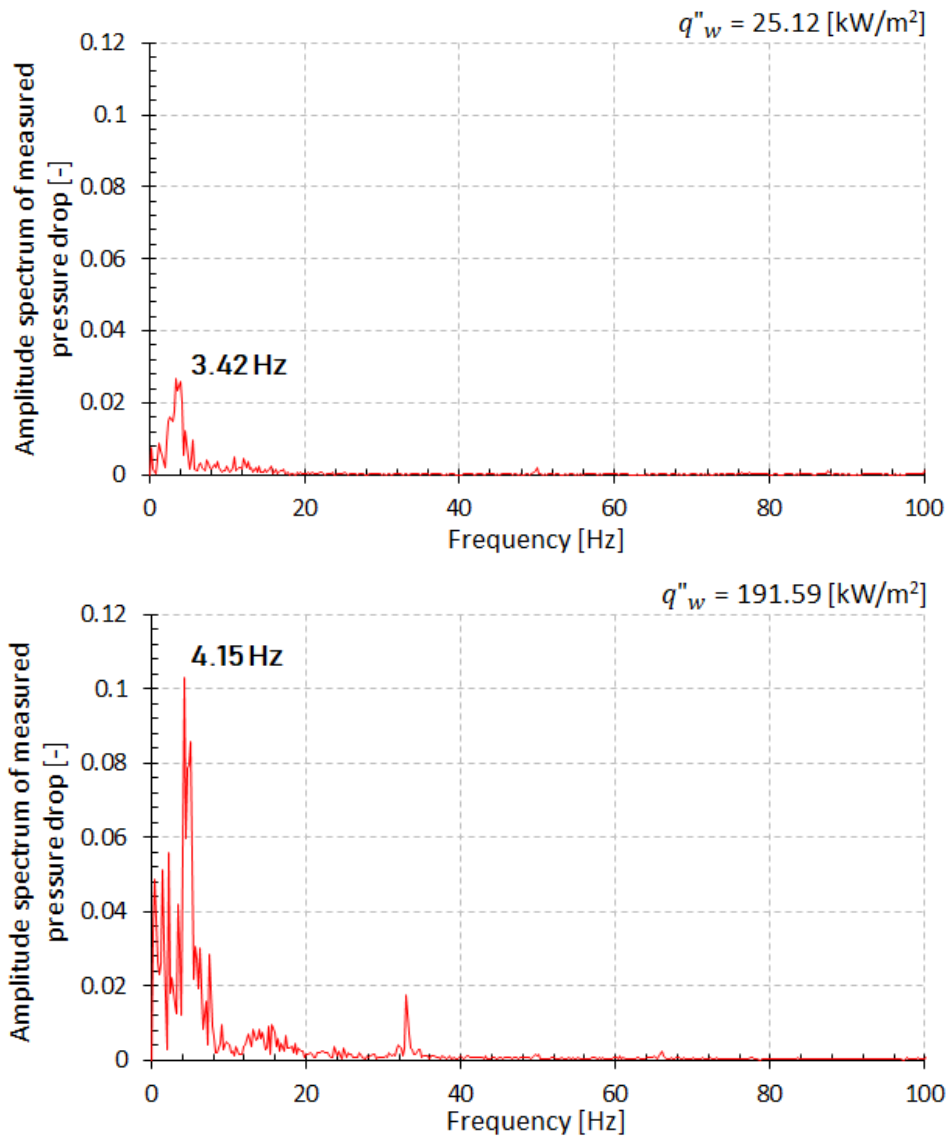


Fig. 23. Frequency analysis of the measured pressure drop at different wall heat fluxes and mass flux of $250 \text{ kg/m}^2\text{s}$.

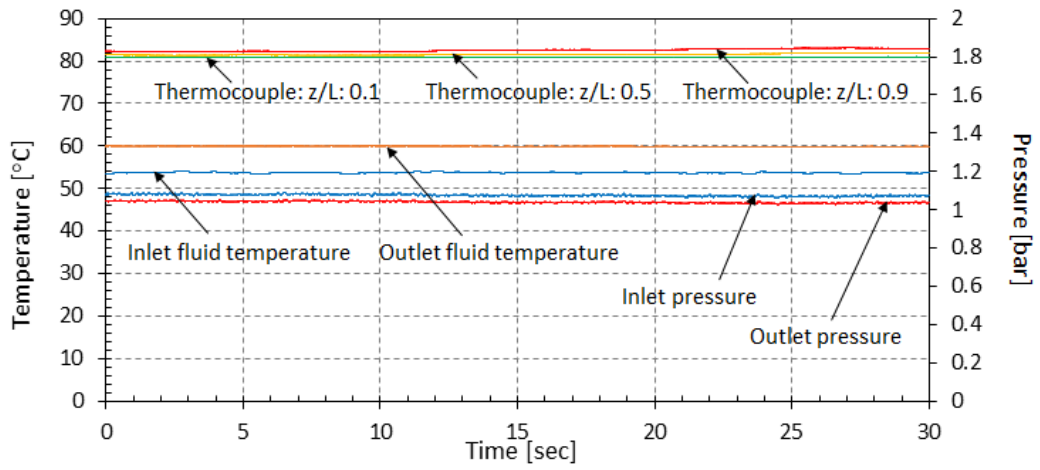


Fig. 24. Pressure and temperature fluctuations at wall heat flux of 191.6 kW/m^2 and mass flux of $250 \text{ kg/m}^2\text{s}$.

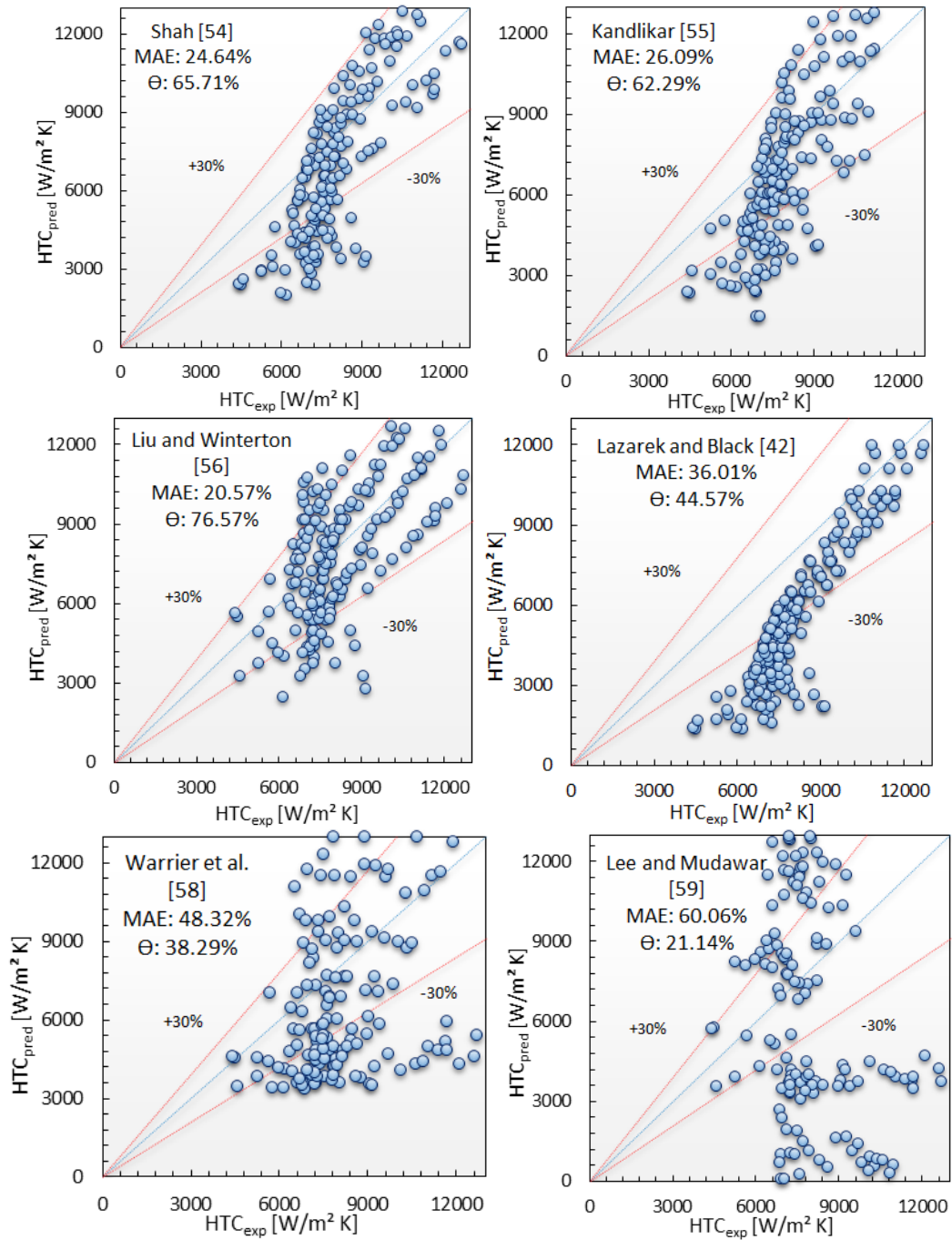


Fig. 25. Comparison with existing flow boiling heat transfer correlations.

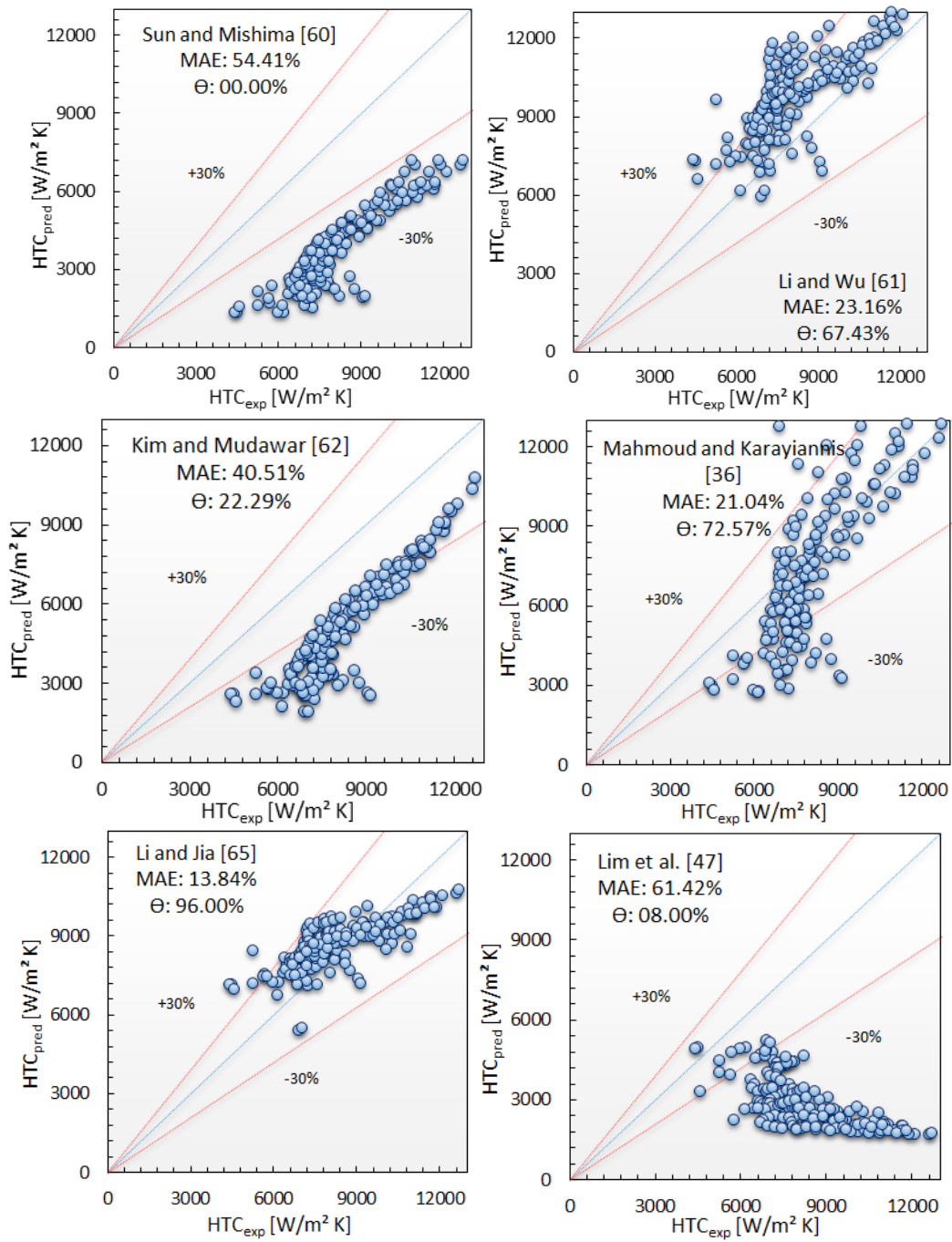


Fig. 25. Continued.

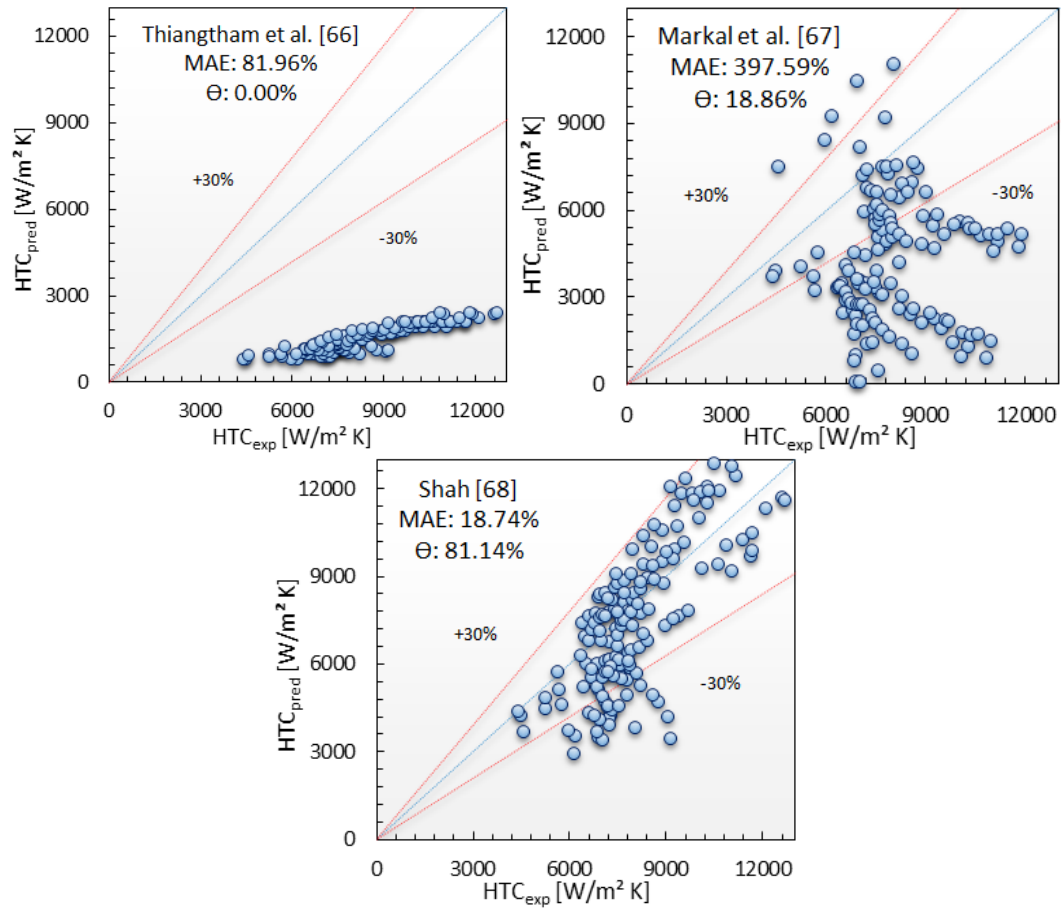


Fig. 25. Continued.

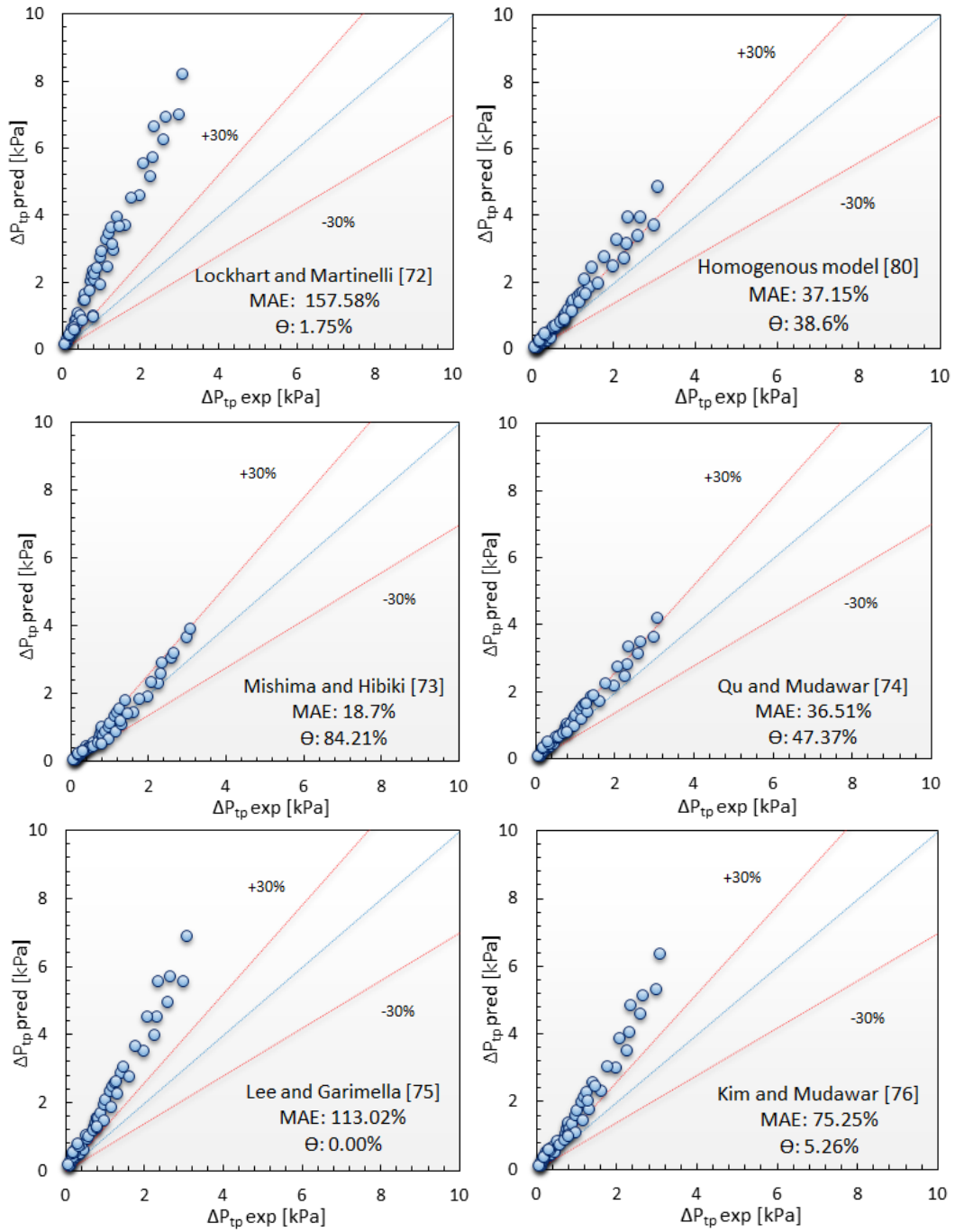


Fig. 26. Comparison with existing two-phase pressure drop correlations.

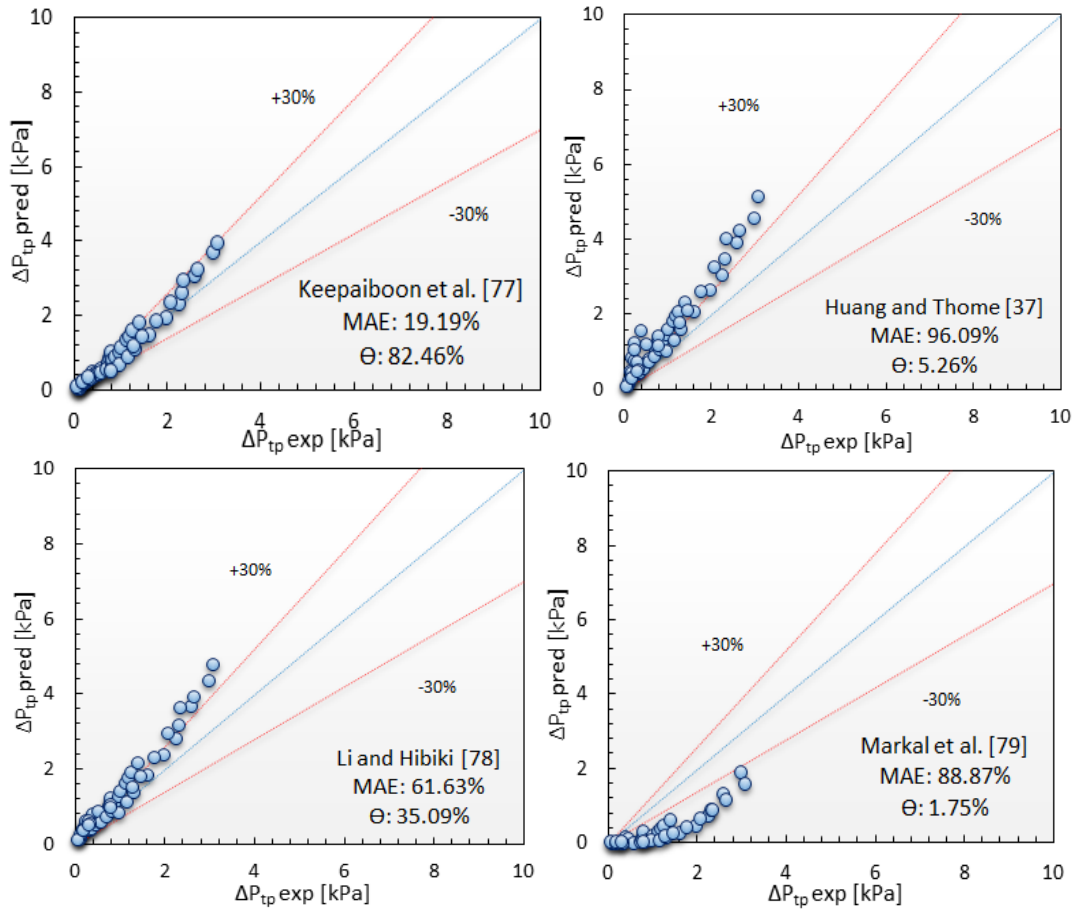


Fig. 26. Continued.